ARTICLE

Check for updates

Structural basis of norepinephrine recognition and transport inhibition in neurotransmitter transporters

Shabareesh Pidathala [1], Aditya Kumar Mallela[1], Deepthi Joseph [1] & Aravind Penmatsa [1✉]

Norepinephrine is a biogenic amine neurotransmitter that has widespread effects on alertness, arousal and pain sensation. Consequently, blockers of norepinephrine uptake have served as vital tools to treat depression and chronic pain. Here, we employ the *Drosophila melanogaster* dopamine transporter as a surrogate for the norepinephrine transporter and determine X-ray structures of the transporter in its substrate-free and norepinephrine-bound forms. We also report structures of the transporter in complex with inhibitors of chronic pain including duloxetine, milnacipran and a synthetic opioid, tramadol. When compared to dopamine, we observe that norepinephrine binds in a different pose, in the vicinity of subsite C within the primary binding site. Our experiments reveal that this region is the binding site for chronic pain inhibitors and a determinant for norepinephrine-specific reuptake inhibition, thereby providing a paradigm for the design of specific inhibitors for catecholamine neurotransmitter transporters.

[1] Molecular Biophysics Unit, Indian Institute of Science, Bangalore, India. ✉email: penmatsa@iisc.ac.in

Neurotransmitter transporters of the solute carrier 6 (SLC6) family enforce spatiotemporal control of neurotransmitter levels in the synaptic space through Na^+/Cl^--coupled uptake in the central and peripheral nervous systems[1–3]. Mono-amine neurotransmitters affect diverse neurophysiological processes, including attention, arousal, sleep, mood, memory, reward, vasodilation, and pain[4–8]. Among monoamines, noradrenaline/ norepinephrine (NE) is an important neurotransmitter released from the neurons of locus coeruleus in the brain stem that innervate multiple regions of the brain and spinal cord[9]. Discovered by vonEuler as a demethylated form of adrenaline[10], NE was identified as a neurotransmitter with agonistic effects on the α- and β- adrenergic receptors[11]. The levels of biogenic amines, NE, dopamine (DA), and serotonin (5-HT), in the neural synapses, are controlled by their cognate transporters, NET, DAT, and SERT, respectively[1,12–15]. Recent structural studies of the *Drosophila* dopamine transporter (dDAT) and the human serotonin transporter (hSERT) reveal that the SLC6 members closely share their architecture and mechanistic properties[16–18]. The structural similarities among biogenic amine transporters extend to overlapping substrate specificities, particularly between DAT and NET, which are both capable of DA and NE uptake, albeit with varying efficacies[19].

Biogenic amine transporters are the primary targets of anti-depressants and psychostimulants that inhibit monoamine transport and enhance neurotransmitter levels in the synaptic space[20,21]. Specific inhibitors of monoamine uptake including selective serotonin reuptake inhibitors (SSRIs), serotonin-norepinephrine reuptake inhibitors (SNRIs), and norepinephrine reuptake inhibitors (NRIs) are widely used to treat depression in comparison with less-selective inhibitors of monoamine transport[22,23]. SNRIs and NRIs are also repositioned and prescribed as medication for chronic pain conditions including neuropathic pain and fibromyalgia[24]. They enhance NE levels in the descending pain pathways innervating the dorsal horn of the spinal cord. In this process, NE-mediated activation of the inhibitory α2-adrenergic receptors lead to lowered Ca^{2+}-channel activation and promote hyperpolarization, to reduce chronic pain[5]. Most inhibitors of monoamine transport competitively inhibit uptake through interactions in the primary binding site[16,25,26]. In addition to interactions at the primary binding site, an allosteric binding site for citalopram that causes non-competitive inhibition of 5-HT transport is observed in the extracellular vestibule of hSERT[27]. This secondary site, in LeuT, a bacterial homolog of neurotransmitter transporters, displays interactions with detergent molecules[28,29]. Instances of non-competitive inhibition are increasingly observed in other neurotransmitter transporters like hDAT[30] and human glycine transporters (hGlyTs)[31].

The primary binding site of biogenic amine transporters is divided into subsites A, B, and C to delineate the regions of the molecule that interact with substrates and inhibitors[32,33] (Fig. 1a). It is also observed that the primary binding site displays remarkable plasticity to accommodate inhibitors of varying sizes[26]. Alteration of the subsite B residues in dDAT to resemble hDAT or hNET yields a transporter with improved affinities to inhibitors including cocaine, β-CFT and the substrate analog 3,4-dichlorophenylethylamine (DCP)[26]. Similarly, the SSRIs also inhibit hSERT through interactions at the primary binding site[17].

Despite recent progress in understanding the pharmacology and transport mechanism of neurotransmitter transporters through dDAT and hSERT structures, questions linger as to whether DA and NE, both catecholamines, have a similar mode of recognition in hNET. Given the lack of an experimental NET structure, it is also confounding as to how inhibitors can be designed with high specificity towards NET over DAT despite sequence identities >65%. In this context, X-ray structures of dDAT in complex with substrates, including DA, DCP, and D-amphetamine, have provided a glimpse into substrate recognition and consequent conformational changes that occur in biogenic amine transporters[26]. Incidentally, dDAT is also capable of NE transport similar to its mammalian orthologues and is well known to have greater affinities towards NE reuptake inhibitors[34,35].

In this study, we employ dDAT as a surrogate of hNET to study the interaction of NE within the primary binding site. Comparison of different dDAT structures including the substrate-free, DA, and NE-bound states allow us to observe and explore interesting differences in substrate recognition in this transporter. Using X-ray structures of dDAT (Supplementary Table 1) in complex with popularly prescribed inhibitors of chronic pain including S-duloxetine, milnacipran, and a synthetic opioid, tramadol, we identify the importance of subsite C as the major determinant of inhibitor specificity between NET and DAT. We also validate these observations through hDAT-like mutagenesis in the subsite C region of dDAT that leads to a loss of affinity towards the NRIs used in the study.

Results and discussion

Modified dDAT resembles hNET primary substrate-binding site. The dDAT, much like its human counterparts hDAT and hNET, is capable of interacting with both DA ($K_i = 2.0\ \mu M$) and NE ($K_i = 19.1\ \mu M$) with varying efficacies (Fig. 2a). The dDAT transports DA with a K_M of 3.6 μM (Supplementary Fig. 1a) and was proposed as a primordial catecholamine transporter in fruit flies[34]. A comparison of dDAT with hNET and hDAT reveals that SNRIs used in the study, duloxetine, milnacipran, and tramadol display inhibition potencies that are similar to hNET in comparison with hDAT (Supplementary Table 2). The amino-acid sequence of dDAT in the primary binding site has high similarity to hNET and hDAT (Supplementary Fig. 1b), and has pharmacological characteristics closer to hNET whilst having better transport characteristics with DA[34]. The dDAT primary binding site is identical to hNET in subsites A and C, whereas it differs by two residues in subsite B with polar substitutions; Asp, instead of Gly, at position 121 (149 in hNET) and Ser, instead of a Met, at position 426 (424 in hNET) (Supplementary Fig. 1b, c). Despite these differences, WT dDAT displays a nisoxetine-binding affinity ($K_d = 5\ nM$) that is very close to hNET ($K_d = 1.9\ nM$)[34,36]. The dissociation constants (K_d) measured for the dDAT constructs, used in this study, also display high-affinity interactions in the range of 2.8–3.8 nM for nisoxetine, similar to hNET (Supplementary Table 2). Besides these, a vestibule-lining phenylalanine in dDAT was mutated to its hNET counterpart leucine (F471L) to make it resemble hNET. The presence of leucine at this site was reported to be important for the specific inhibition of hNET by the χ-conotoxin, MrIA[36]. We investigated the effects of substituting these amino acids in the subsite B and vestibule of dDAT on its transport activity. The vestibular mutation F471L did not result in a significant loss of transport activity (~7%) in comparison with a functional construct of dDAT (dDAT_{fc}). However, introducing D121G substitution led to a 30% reduction in the transport activity, and the S426M mutation resulted in a functionally inactive transporter (Supplementary Fig. 1d). The effect of the two residues on transport activity suggests that the residues in subsite B play a crucial but as yet unidentified role in the transport activity of dDAT.

Despite the inability of dDAT with these mutations in subsite B to transport catecholamines, it is used in this study as it reproduces the binding site of hNET, along with the F471L substitution in the vestibule. This construct, hereafter, referred to as dDAT_{NET} closely resembles the binding propensities of monoamine transport inhibitors with hNET than with hDAT
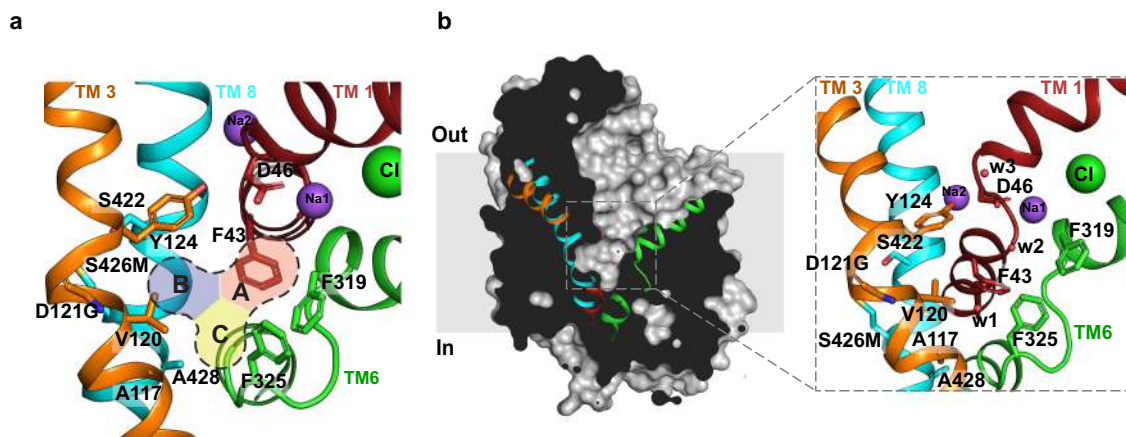
Fig. 1 Organization of primary binding site and substrate-free dDAT. a Close-up view of substrate-free dDAT$_{subB}$-binding pocket, showing the organization of subsites A, B, C of the primary binding site colored as red, blue, and yellow, respectively. **b** Surface representation of substrate-free dDAT$_{subB}$ structure viewed parallel to the membrane plane. Helices TM1, TM3, TM6, and TM8 are colored as red, orange, green, and cyan, respectively. Inset shows the residues lining the primary binding pocket with water molecules indicated as red spheres.
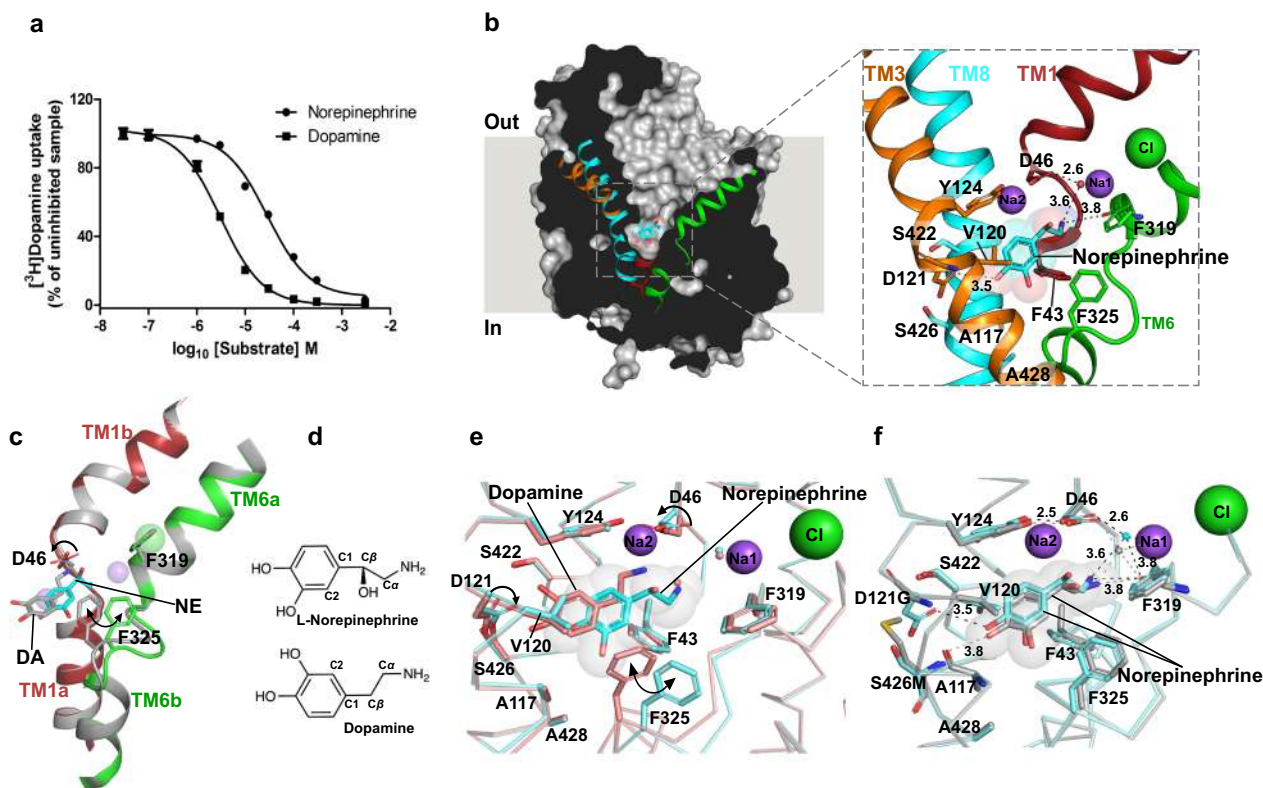

Fig. 2 NE binds in a different pose in comparison with DA-bound dDAT. a Inhibition of [³H] dopamine uptake by dopamine and ʟ-norepinephrine with inhibition constants (K_i) of $2.0 \pm 0.14\,\mu M$ and $19.1 \pm 1.7\,\mu M$, respectively. The data in the plot is a mean of $n = 9$ measurements obtained over three independent experiments and error bars representing s.e.m. **b** Longitudinal section of ʟ-norepinephrine (NE)-dDAT$_{mfc}$ complex with ʟ-norepinephrine displayed as cyan spheres. Close-up view of the ʟ-norepinephrine in the primary binding site with surrounding residues displayed as sticks. Hydrogen bond interactions are depicted as dashed lines. **c** An overlay of TMs 1 and 6 display no change in helix positions, but highlights a shift in the main chain of the TM6 linker (Cα rmsd of 1.4 Å between residues 322 and 326) between the dopamine (DA) bound (gray) and norepinephrine (NE) bound structures (colored helices). **d** Chemical structures of ʟ-norepinephrine and dopamine displayed to highlight differences in binding poses. **e** Comparison of binding pockets of NE-dDAT$_{mfc}$ complex (NE in cyan and backbone in aquamarine) and DA-dDAT$_{mfc}$ (PDB id. 4XP1) complex (DA in deep salmon and backbone in salmon). The D46 sidechain remains in a position similar to antidepressant-bound structures of dDAT (χ^1 torsion angle $+85°$) unlike the dopamine bound structure (χ^1 torsion angle $-175°$). The D121 (TM3) residue in subsite B also shifts (χ^2 shifts by 16°) to interact with NE in comparison with the DA-bound dDAT structure. The position of F325 shifts by nearly 2 Å (Cβ) with a corresponding rotation of the phenyl group by 51° (χ^2 torsion angle CD1-Cγ—Cβ-Cα). **f** Superposition of binding pockets of the NE-dDAT$_{mfc}$ structure (NE and backbone in cyan) with the binding pocket of the NE-dDAT$_{NET}$ structure carrying hNET-like mutations in subsite B (NE and backbone in gray). NE was modeled into densities at near identical positions in both the structures. Source data are provided as a Source Data file.

(Supplementary Table 2). The structure of dDAT$_{NET}$ construct was obtained in its substrate-free, NE-bound, and inhibitor-bound forms. Besides this, a functionally active construct (dDAT$_{mfc}$) (Supplementary Fig. 1d) was also used to obtain a structure complexed with NE. All the crystal structures were obtained in complex with a heterologously expressed, synthetic version of 9D5 antibody fragment (Fab) that was previously used to crystallize the dDAT[16,26,35] (Supplementary Fig. 2).

Substrate-free state is outward-open. The dDAT$_{subB}$ construct, with hNET-like mutations, was crystallized in the substrate-free Na$^+$ and Cl$^-$-bound conformation to observe for structural changes in the binding pocket. The transporter structure, determined at 3.3 Å resolution, displays an outward-open conformation with a solvent-accessible vestibule that is largely devoid of any specifically bound moieties except for the Na$^+$ and Cl$^-$ ions at their respective sites (Fig. 1b). Despite the absence of bound substrate or inhibitor in the primary binding site, multiple blobs of positive density were observed within the extracellular vestibule into which a polyethylene glycol (PEG) was modeled (Supplementary Fig. 3a). Incidentally, the position of PEG coincides with the position of the detergent binding secondary site in LeuT and also with S-citalopram bound allosteric site in hSERT (Supplementary Fig. 3b, c). Within the primary binding site, clear density was observed for most of the residues lining the binding pocket. Solvent accessibility into the primary binding site is unhindered by the F319, which remains splayed open thereby retaining dDAT in an outward-open conformation (Fig. 1b). Interestingly, the sidechain of F325 located in the TM6 linker is positioned in a manner that resembles the antidepressant-bound conformation resulting in a primary binding site with substantial solvent accessibility (Supplementary Fig. 4). A positive density in the vicinity (~3.1 Å) of F325 was observed into which a water molecule was positioned, allowing the F325 to have lone pair-π interactions (Fig. 1b). The outward-open conformation of the dDAT substrate-free state is consistent with the behavior of other NSS members including LeuT whose substrate-free ion-bound conformation is also in the outward-open state[37,38]. The addition of Na$^+$ to LeuT induces the opening of the extracellular vestibule, suggesting the formation of an outward-open state, which is altered upon interactions with substrates like alanine or leucine that induce an occluded state[39]. Recent HDX measurements on dDAT and hSERT have clearly indicated the presence of an outward-open conformation in their ion-bound substrate-free states[40,41]. Similar observations were evident in all-atom simulations performed on a hDAT model built using dDAT as a template[42]. The demonstration of an outward-open conformation in the crystal structure of the substrate-free form of dDAT is a corroboration of these biophysical and computational observations. However, the presence of extraneous factors including a non-specifically bound PEG molecule in the vestibule and the propensity of the antibody fragment to bind an outward-open conformation of the transporter could further aid in stabilizing the substrate-free transporter in an outward-open state.

NE binds in a different pose in comparison with DA. The structural similarity between DA and NE allows them to act as dual substrates for both the NET and DAT orthologues. While the hNET is capable of transporting DA and NE with K_M values of 0.67 μM and 2.6 μM, respectively, the hDAT can transport DA and NE with K_M values of 2.54 μM and 20 μM, respectively[19]. It is consistently observed that both NET and DAT orthologues preferably interact with DA with a higher affinity than NE. It is also observed that in DAT-knockout mice, NET can transport DA and

substitute for its absence[43]. The DA uptake through dDAT can be competed by DA and NE with K_i values of 2.0 μM and 19 μM, respectively (Fig. 2a). These observations validate the use of dDAT as a useful substitute for hNET to study NE interactions.

The NE-bound dDAT$_{mfc}$ structure reveals clear density for NE bound within the primary binding site of the transporter (Fig. 2b, Supplementary Fig. 5a, b). The primary amine of NE interacts in the subsite A region forming hydrogen bonds with carbonyl oxygens of F43 and F319 main chain and the carboxylate sidechain of D46 via a water molecule (Fig. 2b). The D46 residue in the DA-bound dDAT structure undergoes a χ^1 torsion angle shift of 100° relative to that of the NE-bound structure to interact with the primary amine of DA. However, no such shift was observed in the NE-bound dDAT structure (Fig. 2c). The primary amine interacts with a Na$^+$-coordinating water molecule akin to the D-amphetamine and DCP-bound structures (Supplementary Fig. 6). Interestingly, the binding pose of NE does not resemble that of DA in the binding pocket despite both the substrates being catecholamines (Fig. 2c–e). Earlier computational studies predicted that the catechol group of NE predominantly interacts with subsite B region[44,45]. However, we observe that the NE catechol group binds in the vicinity of subsite C in the region between TM6 linker and TM3 with no conformational changes in the binding pocket in comparison with the outward-open substrate-free form of dDAT (Fig. 2b, Supplementary Fig. 6a). The binding of NE in the primary binding site resembles a lock-and-key association in comparison to the induced-fit interaction observed with DA binding. Clear density for the β-OH group of NE is observed in the primary binding site (Supplementary Fig. 5a, b) and the β-OH group faces the solvent-accessible vestibule. The para-OH group of the catechol ring retains interactions with the sidechain carboxyl of D121 that undergoes a rotation of 16° along the χ^2 torsion angle in comparison with the DA-bound structure, to facilitate interactions with NE (Fig. 2e). The meta-OH group of NE displaces the water molecule observed in the substrate-free state, fitting snugly into the gap between A117 and TM6 linker adjacent to the F325 sidechain (Supplementary Fig. 6a). DA, on the other hand, interacts closely with residues in subsite B, displaying a ~180° flip in the position of the catechol group, relative to NE (Fig. 2d, e). This induces a shift in the position of the disordered region of the TM6 linker where the main-chain shifts by a Cα root-mean-square deviation of 1.43 Å for residues 322–326 in the DA-bound structure. This stretch of residues includes a Gly-Pro-Gly motif with the G324 displaying the maximal Cα deviation of 2.4 Å, allowing the F325 (Cα shift of 1.6 Å) to facilitate edge-to-face aromatic interactions with DA, which are absent in the NE-bound structure (Fig. 2c, e, Supplementary Movie. 1). Shifts in the TM6 linker have been observed before and are vital to remodel the binding site in response to substrate and inhibitor interactions[26,46].

The subsite B residues in dDAT differ from hNET and hDAT at two positions, D121G (TM3) and S426M (TM8) (Supplementary Fig. 1b, c). In order to evaluate whether hNET-like substitutions in the subsite B of dDAT would influence and shift the conformation of NE to DA-like pose, we crystallized NE in complex with dDAT$_{NET}$ construct that has D121G and S426M substitutions, alongside F471L. Despite hNET-like substitutions, no major shifts in the position of NE were observed in the binding site. Despite absence of the D121 sidechain, the para-OH group of NE establishes interactions with the main-chain carbonyl oxygen of A117 (Fig. 2f).

The comparison between DA and NE-bound crystal structures displays an unexpected difference between preferred conformers of DA and NE within the binding pocket. The catechol ring of NE is positioned in opposite orientation relative to that of DA with a

minor difference in the C_2C_1-$C_\beta C_\alpha$ torsion angle (26°) (Fig. 2d). This difference in their binding poses, despite being very similar catecholamines, can be attributed to the presence of β-OH group in NE, which restricts the rotation of its catechol ring along the C_1–C_β bond with an energy barrier of 9–12 kcal/mol[47]. In the case of DA, the energy barrier for the same rotation is as low as 0.3–0.6 kcal/mol[48]. The low energy barrier for the rotation of the catechol group in DA allows greater conformational sampling and enables it to interact in close proximity to the subsite B of the primary binding site. On the other hand, the energy barrier for catechol rotation in NE, owing to the β-OH group, restricts its pose such that it is oriented more towards subsite C relative to DA and results in a relatively weaker interaction with the transporter. The binding of DA to dDAT results in an inward movement of the non-helical linker between TM6a-TM6b by 1.43 Å relative to that in the NE-bound state (Supplementary Movie 1). The induced-fit conformational change in response to DA binding likely leads to larger binding free energy changes, primarily caused by conformational changes and the formation of non-covalent interactions within the binding site yielding larger enthalpy differences, upon binding[49]. In the case of NE, interaction in the binding site results in the displacement of water with no consequent conformational changes, therefore resembling a lock-and-key association. We can therefore infer that the difference in flexibility of the two catecholamines, caused by the β-OH group, translates to both DAT and NET to have a greater propensity to interact with DA in comparison to NE.

S-duloxetine and milnacipran are competitive inhibitors of NE transport. The ability of SNRIs to alleviate chronic pain by blocking NET activity in the descending pain pathways has allowed drugs like S-duloxetine and milnacipran to be repositioned for treatment of neuropathic pain and fibromyalgia[50]. Much like the other inhibitors/antidepressants characterized including nortriptyline, nisoxetine, and reboxetine in complex with dDAT[16,35] and paroxetine, S-citalopram, fluoxetine in complex with hSERT[51], both S-duloxetine and milnacipran interact at the primary binding site of the dDAT structure (Figs. 3, 4). The electron densities for both drugs are unambiguous and conform to the general principles of inhibitor interactions with the transporter (Supplementary Fig. 5c, d).

S-duloxetine, owing to its large surface area (surface area 505.7 Å^2) exhibits maximal occupancy of the primary binding pocket. The drug inhibits DA uptake with a K_i value of 69.4 ± 2.9 nM (Fig. 3a), consistent with the K_i values observed for hNET inhibition by duloxetine[32]. The high affinity is an outcome of its ability to snugly fit into the cavernous primary binding site of NSS transporters. In duloxetine, the propanamine group interacts with the main-chain carbonyl oxygens from residues F43 and F319 with the D46 residue in the vicinity (Fig. 3b). The secondary amine can also mediate π–cation interaction with the sidechain of F43. The naphthyloxy ring interactions in the binding pocket extend from subsite B to subsite C, wedging into space sculpted by residues including Y124, D121G, S426M, V120, A117 in TM3 and TM8 followed by edge-to-face aromatic interactions with
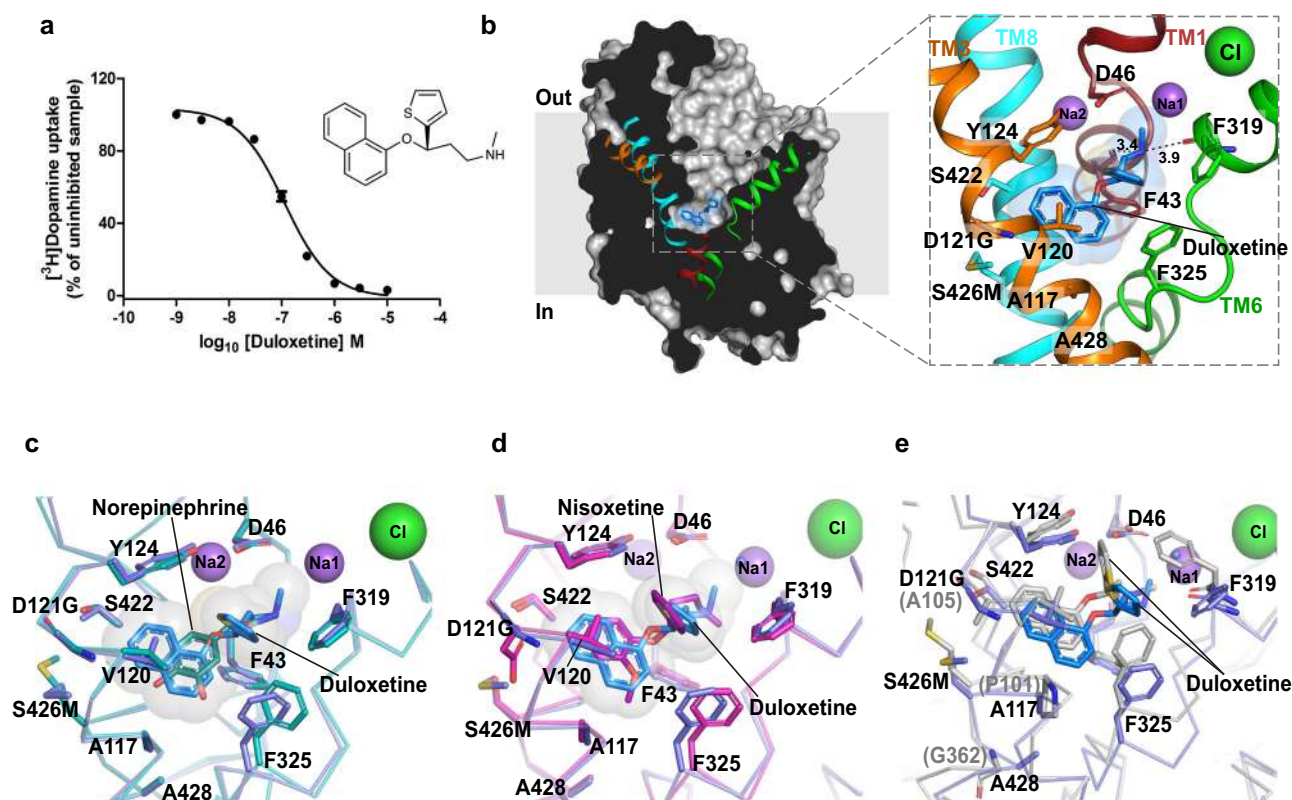

Fig. 3 S-duloxetine binds in the primary binding site. a Inhibition of [³H] dopamine uptake with S-duloxetine with a K_i of 69.4 ± 2.9 nM (data in the plot is a mean of $n = 9$ measurements obtained over three independent experiments and error bars representing s.e.m.). **b** Surface representation of dDAT$_{subB}$ with bound S-duloxetine shown as blue sticks and transparent spheres in the primary binding site. Inset shows orientation of the inhibitor in the binding pocket with residues in the vicinity represented as sticks. **c** Binding site comparison of S-duloxetine with NE-bound dDAT$_{NET}$. The phenyl group of F325 shifts by 40° to retain edge-to-face aromatic interactions with the naphthalene group of S-duloxetine. **d** Overlay of the dDAT bound to S-duloxetine and nisoxetine (magenta) (PDB id. 4XNU). The surrounding residues display an identical binding pose between the two structures. **e** Overlay of duloxetine-bound dDAT$_{subB}$ and LeuBAT structures (gray) (PDB id. 4MMD) displaying similar pose of the inhibitor in both the structures. LeuBAT displays a prominent occluded conformation, whereas dDAT retains an outward-open conformation. Source data are provided as a Source Data file.
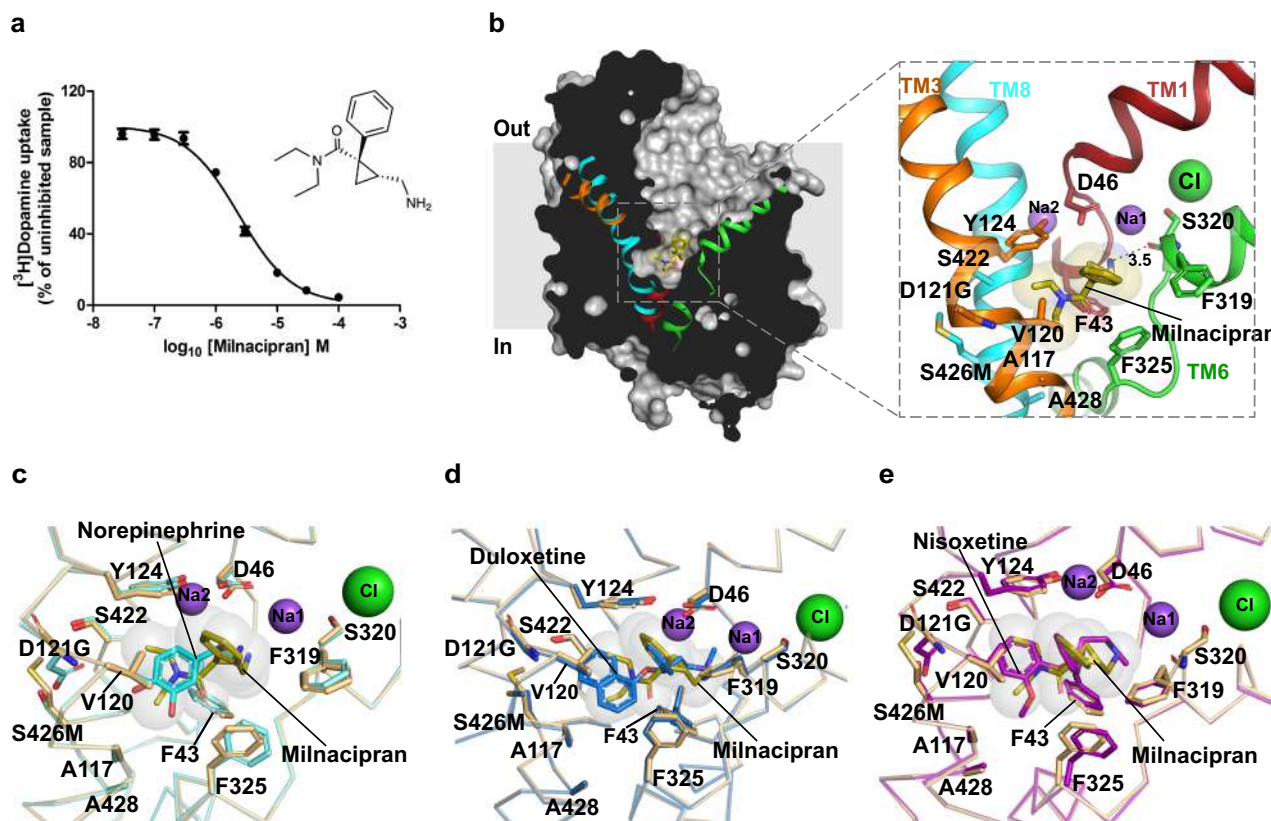
Fig. 4 Milnacipran is a competitive inhibitor of NE uptake. a [³H] dopamine transport inhibition by increasing concentrations of 1R-2S milnacipran with a K_i value of $1.5 \pm 0.1 \mu M$ (data in the plot are a mean of $n = 9$ measurements obtained over three independent experiments and error bars representing s.e.m). Inset displays the chemical structure of 1R-2S milnacipran. **b** Longitudinal section of dDAT$_{NET}$ in complex with milnacipran-bound (olive sticks) in the primary binding site with residues in proximity displayed as sticks. **c** Milnacipran-binding pose compared with NE binding in dDAT$_{mfc}$ reveals an angular shift of F325 by 35° to retain hydrophobic interactions with the diethyl group of milnacipran. **d** Milnacipran-bound dDAT$_{NET}$ vs duloxetine-bound dDAT$_{subB}$ display identical positions of the surrounding residues. **e** Structural overlap of nisoxetine bound dDAT (PDB id. 4XNU) with milnacipran-bound dDAT$_{subB}$, revealing the surrounding residues in identical binding positions. Source data are provided as a Source Data file.

F325 in subsite C. The thiophene ring is positioned with some elevation within the binding pocket to sterically block the closure of the F319 and thus precluding the formation of an occluded state during transport (Fig. 3b). The duloxetine position in the binding pocket overlaps with NE and nisoxetine binding to a large extent with the naphthalene ring taking the place of the methoxyphenyl ring of nisoxetine, a specific inhibitor of NE reuptake (Fig. 3c, d). Similarly, when compared with the cocaine-bound structure of dDAT, one of the aromatic groups of the naphthalene ring in duloxetine overlaps with the benzoyl moiety of cocaine (Supplementary Fig. 7). However, the lack of an additional hydrophobic moiety in cocaine makes it a moderate inhibitor of NE uptake, relative to duloxetine[52]. The position of duloxetine in the binding pocket is very similar to the LeuBAT-duloxetine complex elucidated earlier, thus corroborating Leu-BAT as a relevant model system to study the pharmacology of biogenic amine transporters (Fig. 3e)[33].

Milnacipran has an unconventional structure with a cyclopropyl skeleton having both a primary amine and tertiary amine (N, N-diethyl) being part of the drug structure[53]. The drug lacks large aromatic moieties that are commonly observed with most NSS inhibitors. Milnacipran inhibits DA transport by dDAT with a K_i value of $1.5 \pm 0.1 \mu M$, which is much higher than S-duloxetine (Fig. 4a). Like duloxetine, milnacipran also binds in the primary binding site and overlays well with NE (Fig. 4b, c). The primary amine of aminomethyl group in milnacipran interacts with the sidechain of D46 and the main-chain carbonyls

of F43 and S320 in the subsite A by hydrogen bonds (Fig. 4b). Altering the hydrophobicity of the binding site by substituting residue V148 (V120 in dDAT$_{NET}$) in hNET to an isoleucine leads to a 17-fold enhancement of milnacipran's inhibitory potency[32]. The phenyl group attached to the chiral center at the cyclopropane group overlaps with the thiophene group of duloxetine and phenyl ring of nisoxetine (Fig. 4d, e). Interestingly, the N, N-diethyl group, which is usually occupied by bulky aromatic groups in most of the inhibitors, does not wedge deeply into the subsite B as observed with cocaine (Supplementary Fig. 7c) and retains hydrophobic interactions in the vicinity of subsite C. The absence of a bulky aromatic group wedging into subsite B could be the reason for the lowered transport inhibition observed in milnacipran in comparison to duloxetine (Supplementary Table 2).

Synthetic opioid tramadol blocks transport by interacting with subsite C. It is well known that some synthetic opioids have a dual mechanism of action for pain relief by serving as agonists of μ-opioid receptors and blockers of NE and 5-HT uptake. Tramadol is a popularly used synthetic opioid with a dual ability to activate opioid and NE-based analgesic pathways[54]. Although tramadol is considered a safe drug, it induces opioid-like symptoms and dependence when used in supra-therapeutic doses[55]. The demethylated metabolite of tramadol, o-desmethyl tramadol (desmetramadol) is a better agonist for opioid receptor whilst
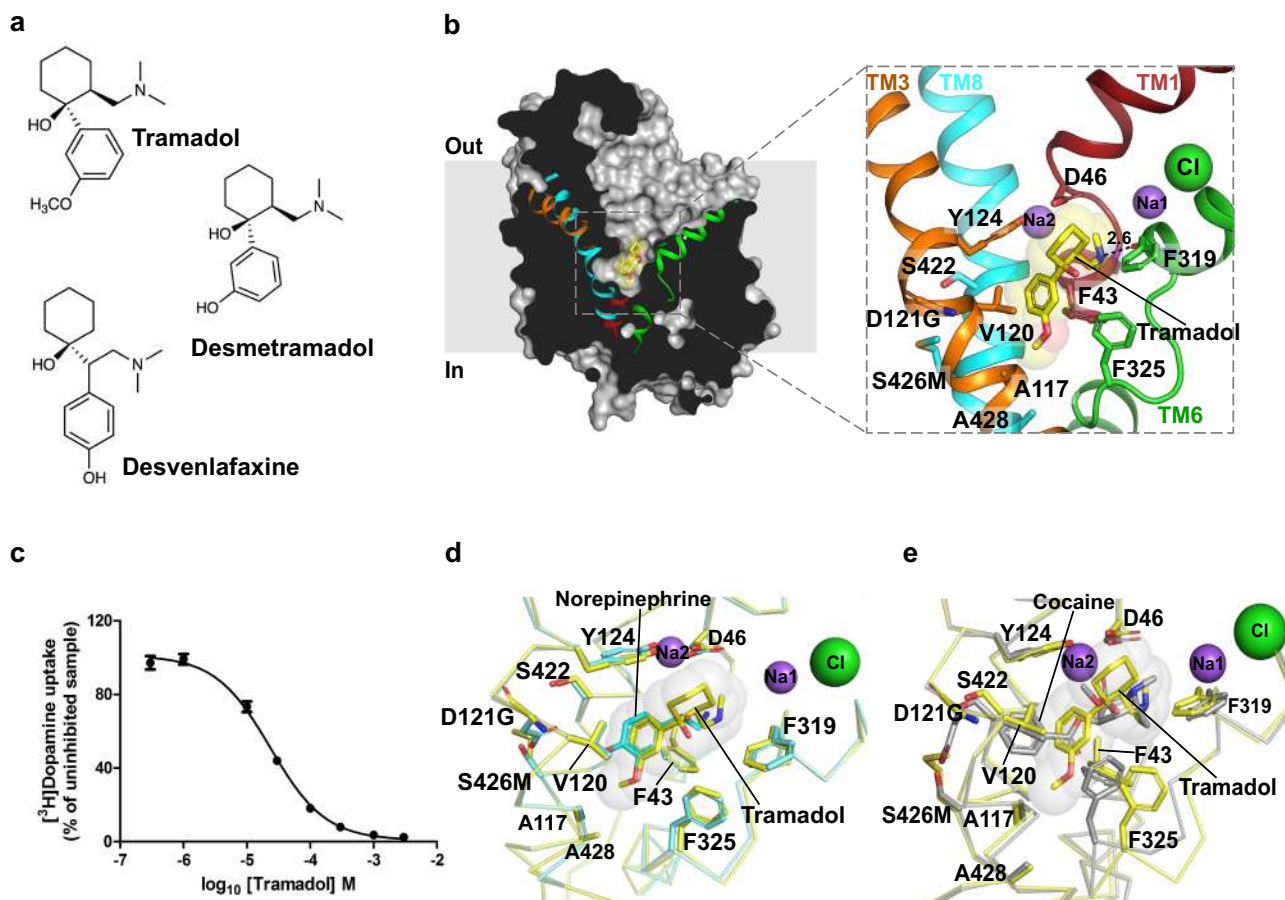
Fig. 5 Tramadol is a synthetic opioid that inhibits NE uptake. a Chemical structures of inhibitors, tramadol, desmetramadol, and desvenlafaxine. **b** Structure of tramadol (yellow) bound dDAT$_{NET}$ viewed parallel to the membrane plane where tramadol was observed in the primary binding site. **c** [^{3}H] dopamine uptake inhibition observed with increasing concentrations of tramadol displaying a K_i value of 15.9 ± 1.8 µM (data in the plot is a mean of $n = 9$ measurements obtained over three independent experiments and error bars representing s.e.m). **d** Structural comparison around the primary binding site between tramadol bound dDAT$_{NET}$ and NE-bound dDAT$_{mfc}$ wherein the methoxyphenyl group of tramadol overlaps exactly with the catechol ring of NE. No differences in the positions of the binding site residues were observed. **e** Comparison of tramadol-bound dDAT$_{NET}$ structure with cocaine-bound dDAT$_{mfc}$ structure (gray) (PDB id. 4XP4). The benzoyl ester group of cocaine clearly interacts with subsite B, whereas tramadol's aromatic group interacts primarily at subsite C, within the primary binding site. Source data are provided as a Source Data file.

tramadol, particularly S,S-tramadol is specific to NE transport inhibition[56]. Tramadol and desmetramadol structurally resemble the antidepressant, desvenlafaxine (Fig. 5a). Tramadol inhibits the transport activity of dDAT with a K_i of 15.9 ± 1.8 µM (Fig. 5), which is substantially higher than that of S-duloxetine and milnacipran, indicating weaker affinity. Similarly, tramadol has higher K_i value of 5.3 ± 0.4 µM relative to the other studied inhibitors for competitively displacing nisoxetine from the binding pocket (Supplementary Fig. 8). Despite weaker affinities to the transporter, tramadol is highly specific to NET/SERT over DAT displaying ~50-fold greater affinity to NET over DAT[56]. The structure of the tramadol–dDAT$_{NET}$ complex reveals that the drug binds to the primary binding site with the tertiary amine of the dimethylamino group interacting with subsite A residues D46 and carbonyl oxygens of F43 and F319 (Fig. 5b, Supplementary Fig. 5e). The 1-cyclohexanol group takes a similar position to the thiophene group of S-duloxetine and phenyl groups of milnacipran and nisoxetine to sterically prevent the formation of an outward-occluded conformation in the transport process (Supplementary Fig. 4). The lower affinity of tramadol to inhibit neurotransmitter uptake compared with other SNRIs could be attributed to the lack of an aromatic moiety in the close vicinity of the subsite B. This distinction is even more apparent when the tramadol bound dDAT$_{NET}$ structure is compared with cocaine-

bound dDAT$_{mfc}$ structure where the benzoyl group of cocaine is clearly wedged into subsite B in comparison with tramadol's methoxyphenyl ring that is primarily in the vicinity of subsite C (Fig. 5e). The methoxyphenyl ring interacts with the sidechain of Y124 by aromatic edge-to-face interactions and fits into the hydrophobic pocket lined by the side-chains of A117, V120, A428, and F325 of subsite C. The position of methoxyphenyl group coincides very closely with the catechol group of NE and methoxy group overlaps well with the meta-OH of NE (Fig. 5d). Much like nisoxetine and reboxetine, the methoxy group of tramadol occupies the space between A117 and F325. Interestingly, the demethylated metabolite of tramadol, desmetramadol is a weaker inhibitor of hNET (IC$_{50}$ = 6 µM) relative to tramadol (IC$_{50}$ = 2 µM)[56]. This indicates the importance of this hydrophobic interaction in enhancing the efficacy of selective NE reuptake inhibition. A close examination of the binding pocket reveals that hDAT and hNET have subtle differences within them. The dDAT, although largely resembling hNET in the binding pocket, differs from hDAT in the residues A117(TM3), S422(TM8), and A428(TM8). A117 and A428 residues line subsite C in the vicinity of the TM6 linker where NET-specific drugs like nisoxetine, reboxetine, milnacipran, and tramadol interact. The lack of interactions in subsite B and the presence of substitutions in subsite C (A117S and A428S) unique to human
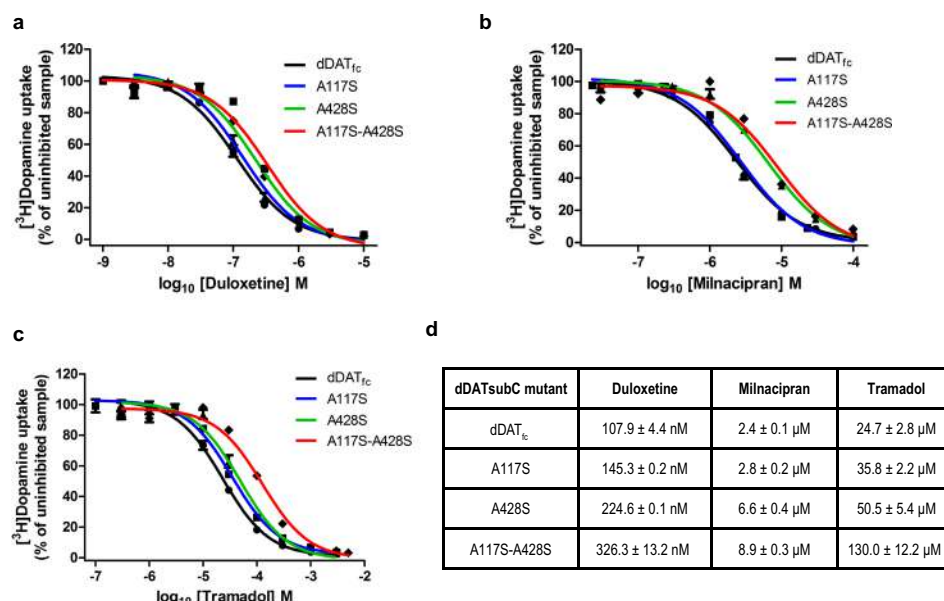
Fig. 6 hDAT-like mutagenesis of residues leads to reduced affinities of NET-specific inhibitors. a Dose–response curves of [^{3}H] dopamine uptake inhibition by duloxetine with a functional construct of dDAT carrying hDAT-like mutations in the primary binding site including dDAT functional construct (dDAT$_{fc}$) (black), A117S (blue), A428S (green), and A117S/A428S double mutant (red). The uptake inhibition curves of subsite C mutants were compared with that of the dDAT$_{fc}$ (black) plots shown in previous figures. **b**, **c** Similar uptake inhibition curves plotted using milnacipran and tramadol, respectively. Experimental plots for all mutants are means of $n = 9$ measurements obtained over three independent experiments and error bars representing s.e.m. **d** Table indicates IC$_{50}$ values ± s.e.m of individual mutant inhibition curves with all three inhibitors. Substitution of subsite C residues A428S and double mutant A117S and A428S display maximal loss of affinity for SNRIs duloxetine, milnacipran, and tramadol. The loss in inhibition potencies is significant (p values for duloxetine, milnacipran, and tramadol are 2.44×10^{-8}, 6.03×10^{-10}, and 1.43×10^{-5}, respectively) between the dDAT$_{fc}$ and the dDAT A117S-A428S mutant. A two-tailed t test assuming unequal variances was performed to obtain the p values. Source data are provided as a Source Data file.

DAT, makes tramadol a weak hDAT inhibitor with a IC$_{50}$ of ~100 μM[56]. Tramadol exhibits similar K_i values for displacing nisoxetine bound to dDAT$_{mfc}$ and dDAT$_{NET}$ proteins wherein dDAT$_{NET}$ has hNET-like D121G/S426M substitutions in subsite B (Supplementary Fig. 8). In contrast, inhibitors like cocaine, which primarily bind to subsite B have a 10-fold increment in their ability to compete for nisoxetine in the presence of hNET-like mutations in subsite B[26]. The observations from tramadol-dDAT complex clearly indicate that NET-specific inhibition occurs through interactions at subsite C. It is also evident that the lack of interactions at subsite B compromises the affinity of tramadol, but clearly fails to influence the specificity of NET inhibition in comparison with DAT[56].

Ligand binding to subsite C influences specificity of NE uptake inhibition. The structures of SNRIs duloxetine, milnacipran, and tramadol in complex with the dDAT show a progressively smaller aromatic moiety that interacts with the subsite B and C in the primary binding pocket of dDAT. In an earlier study, it was observed that the aromatic moieties in drugs like cocaine, RTI-55, and nisoxetine interact closely in the subsite B and have enhanced affinities when hNET-like substitutions D121G and S426M are made in the pocket[26]. Interestingly, this improvement in affinity is not apparent in the case of SNRIs employed in the study where the K_i values remain unchanged or weaken when substitutions in subsite B are made to improve the identity of dDAT-binding pocket to hNET (Supplementary Fig. 8). The minimal effect of subsite B substitutions on the affinity of duloxetine, milnacipran, and tramadol suggest that determinants of NET specificity lie elsewhere in the binding pocket. Earlier studies have posited that non-conserved residues in the primary binding site are responsible for selective inhibition of biogenic amine uptake[57,58]. In

order to evaluate the role of the subsite C residues that differ between hNET and hDAT in the binding site, hDAT-like mutations A117S, A428S and a combination of A117S/A428S were introduced into $dDAT_{fc}$. Effects of these mutations were analyzed through uptake inhibition using the three SNRIs employed in this study (Fig. 6a–c). Individual substitution of A428S at subsite C caused a marginal (two–threefold) loss of uptake inhibition, whereas the A117S mutation did not cause any significant change (Fig. 6d). However, a combination of A428S and A117S caused a substantial loss in the ability of duloxetine, milnacipran, and tramadol to inhibit DA transport as observed by a ~3, ~3.8, and ~5-fold increase in their IC$_{50}$ values, respectively (Fig. 6d). The IC$_{50}$ value for tramadol obtained with the A117S-A428S double mutant is very similar to its reported IC$_{50}$ value with hDAT (Fig. 6d; Supplementary Table 2)[56,59]. Thus, these substitutions clearly indicate the importance of subsite C region in dictating the specificity of individual inhibitors that exploit this hydrophobic cavity to gain NET specificity. The polar substitutions observed in this region in hDAT lead to a reduced ability of SNRIs with hydrophobic moieties to bind efficiently, thereby compromising their ability to interact with the hDAT (Fig. 7a, b).

In conclusion, using X-ray structures of dDAT in complex with NE and NET-specific inhibitors, highlights the discrepancies in catecholamine recognition in neurotransmitter transporters and explores the basis for NET-specific reuptake inhibition over DA reuptake inhibition, despite the close similarity between NET and DAT. The catechol group of NE is observed to interact primarily at subsite C in the vicinity of NET-specific residues A117 and A428. The binding of NE displaces water molecules in the binding pocket observed in the substrate-free state and does not induce any local conformational changes in the binding, contrary to DA (Fig. 7a). DA was previously observed to interact closely with its catechol group in the vicinity of subsite B, leading to
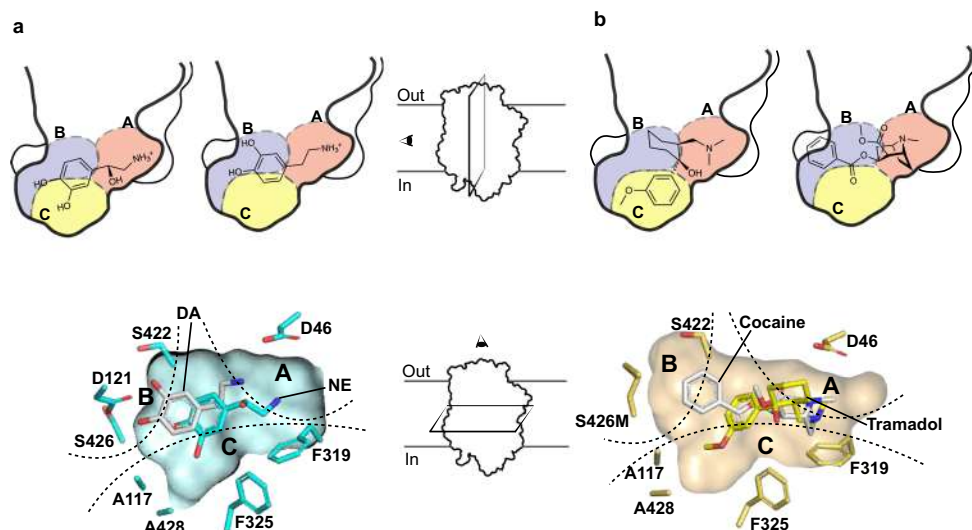
Fig. 7 Distinct binding poses of substrates and NET inhibitors. a Lateral sections of the primary binding pocket comparisons between NE and DA-bound states reveal distinct conformations and binding poses of the two substrates in the subsite C and subsite B, respectively (top). Transverse section of the binding pocket clearly reveals similar distinctions between NE and DA (bottom). **b** Lateral section comparisons between tramadol and cocaine, displaying primary interactions of their aromatic moieties in subsite C and subsite B, respectively (top). Transverse section of the binding pocket showing tramadol overlapped with cocaine indicates clear differences in interaction of a non-specific inhibitor, cocaine towards subsite B and an SNRI, tramadol interacting preferentially with subsite C.

shifts in the positions of residues D46 and F325 to retain interactions with the neurotransmitter[26]. The absence of these changes in NE-dDAT complex could be attributed to the reduced flexibility of NE, in comparison with DA, owing to the presence of the β-OH group in its structure[47].

The NET-specific chronic pain inhibitors, duloxetine, milnacipran, and tramadol, compete for NE-binding site through aromatic groups. These aromatic moieties can interact and snugly fit at subsites B and C to retain high affinity and selectivity towards specific biogenic amine transporters. However, hDAT-like mutations within subsite C of dDAT, A117S, and A428S alter the polarity of the binding pocket and weaken the hydrophobic interactions and prevent functional groups like the methoxyphenyl group of tramadol from accessing the subsite through steric block (Fig. 7b). On the other hand, non-specific inhibitors of biogenic amine transport, for instance cocaine, primarily interact with subsite B wherein hNET-like mutations D121G and S426M in dDAT enhance cocaine affinity by 10-fold. The primary interactions of cocaine at subsite B induces a plastic reorganization of the binding pocket as the subsite C residue F325 compensates for lack of bulky aromatic group in cocaine through local conformational changes to establish aromatic π-stacking interactions[26]. Through our results, we infer that NET-specific inhibitors could be designed with primary interactions at subsite C whilst non-specific high-affinity interactions are observed in inhibitors that interact at subsite B. Taken together, the results of this work convey the unique facets of catecholamine recognition within the same binding pocket and establish the roles of individual subsites in dictating inhibitor selectivity and affinity among biogenic amine transporters. The findings can effectively be used for selective inhibitor design targeting pharmacological niches as widespread as depression and chronic pain.

Methods

List of constructs. The *Drosophila melanogaster* DA transporter construct used for performing transport assays (*dDAT_{fc}*) has a deletion of 20 amino acids in the amino-terminal (Δ1–20) and a deletion in the extracellular loop 2 (EL2) from 164 to 191 amino acids. It also contains two thermostabilizing mutations V74A, L415A, and F471L mutation in the vestibule to resemble human norepinephrine

transporter (hNET). Additional mutations in the subsite B or subsite C were incorporated into this gene used for carrying out the uptake assays.

The uptake active *dDAT* construct used for co-crystallizing with NE (*dDAT_{mfc}*) has amino-acid deletions Δ1–20 and Δ162–202 along with the two thermostabilizing mutations (V74A and L415A). A thrombin site (LVPRGS) insertion replaces residues 602–607 towards the C-terminus. It also has the F471L mutation in the vestibule (Supplementary Table 3).

dDAT_{subB} has deletions Δ1–20 and Δ162–202; thermostabilizing mutations V74A, L415A along with two mutations in subsite B of the substrate-binding pocket D121G and S426M (Supplementary Table 3). A thrombin site insertion, identical to *dDAT_{mfc}* is present in the C-terminus. This construct was used to elucidate the crystal structures of substrate-free and the duloxetine bound form.

dDAT_{NET} is identical to *dDAT_{subB}* with the additional mutation F471L in the vestibule. This construct was used to decipher the crystal structures in NE, milnacipran, and tramadol bound complexes of dDAT.

Expression and purification of the transporter. The recombinant expression of *dDAT* constructs in pEG-BacMam vector was done using baculovirus-mediated protein expression in mammalian cells, where HEK293S GnTI− cells were transduced with high titer recombinant baculovirus using the BacMam method[60]. The expressed dDAT protein was extracted from membranes in 20 mM dodecyl maltoside (DDM) (Anatrace), 4 mM cholesteryl hemisuccinate (CHS) (Anatrace), 50 mM Tris-Cl (pH 8.0), and 150 mM NaCl. The solubilized material was centrifuged at $100,000 \times g$ to pellet down the unsolubilized material. The solubilized protein was affinity-purified using Talon resin (Takara Bio) in 20 mM Tris-Cl (pH 8.0), 300 mM NaCl, 100 mM imidazole containing 1 mM DDM, and 0.2 mM CHS. The affinity-purified protein was treated with thrombin (Haematologic Technologies Inc) for removing the C-terminal GFP-8x-His tag. The thrombin cleaved protein was purified by size-exclusion chromatography on a superdex-200 10/300 increase column (GE Life Sciences) in 4 mM decyl β D-maltoside (Anatrace), 0.3 mM CHS, 0.001% (w/v) 1-pamitoyl-2-oleoyl-*sn*-glycero-3-phospho ethanolamine (Avanti Polar Lipids), 20 mM Tris-Cl (pH 8.0), 300 mM NaCl, and 5% glycerol. The peak fractions were collected and pooled before incubating with the substrate (6 mM) or inhibitor (0.5–2.0 mM) to the indicated final concentrations used for crystallization. For complexes containing NE (Sigma Aldrich), 4 mM ascorbic acid (Sigma Aldrich) was added to prevent its oxidation.

Heterologous expression and purification of Fab. The heavy and light chain genes of the *Fab 9D5* were synthesized (Genscript) and cloned into pFastBac Dual vector with the heavy chain under the polyhedrin promoter and the light chain under the P10 promoter with an N-terminal GP64 signal peptide on each chain. A TEV protease site followed by 8x-His tag was added to the C-terminus of heavy chain. The cloned plasmid was transformed into *Escherichia coli* DH10Bac (Thermo Fischer Scientific) for the generation of recombinant bacmids. The bacmids were then transfected into Sf9 cells (Invitrogen) to generate recombinant baculovirus. High titer recombinant virus was used to infect large volume Sf9 cell cultures and 96 h post infection, the cells were spun down and the supernatant

containing Fab was dialyzed against 25 mM Tris-Cl (pH 8.0) and 50 mM NaCl. The dialysate was then passed through Ni-NTA beads (Qiagen), washed with 50 mM imidazole and eluted in 25 mM Tris-Cl (pH 8.0), 50 mM NaCl containing 250 mM imidazole. The eluted Fab was further purified by size-exclusion chromatography in 25 mM Tris-Cl (pH 8.0) and 50 mM NaCl using a superdex 75 10/30 column (GE Life Sciences). The purified Fab was stored at 4 °C.

Crystallization and structure determination. The SEC-purified dDAT was incubated with varying concentrations of ligands for 2–4 h at 4 °C before incubating with the recombinant antibody fragment (Fab) 9D5 in a molar ratio of 1:1.2 (dDAT:Fab) for 30 mins on ice. The dDAT-9D5 complex was concentrated to a final concentration of 3.0–4.0 mg/ml using a 100 kDa cutoff centrifugal concentrator (Amicon Ultra). The concentrated sample was clarified to remove aggregates by high-speed centrifugation at $14,500 \times g$ for 30 mins. The clarified sample was then subjected to crystallization by hanging-drop vapor diffusion method at 4 °C. Crystals of $dDAT_{subB}$ and $dDAT_{NET}$ proteins were obtained after 2–4 weeks, whereas those for $dDAT_{mfc}$ were obtained in a week after seeding the crystallization drops with the $dDAT_{NET}$ crystals. All crystals were obtained in 0.1 M MOPS, pH 6.5–7.0 and 30–32% PEG 600 as precipitant at 4 °C. Data from crystals were collected at different synchrotrons sources (Supplementary Table 1) and crystals for all data sets diffracted in a resolution range of 2.8–3.3 Å. The diffraction data were processed using XDS[61] and merged and scaled using AIMLESS in the CCP4 software suite[62]. Five percent of the reflections were randomly assigned for R_{free} calculations as part of cross-validation. The structures were solved by molecular replacement through PHASER[63] using the coordinates of dDAT and 9D5 from PDB ids 4XP1 or 4XNX. Refinement of the coordinates against the diffraction data were done using phenix.refine in the PHENIX crystallographic software suite[64]. Protein and inhibitor structures were built using COOT[65] and modeling for lower resolution datasets was done with the aid of feature-enhanced map employed in the PHENIX suite[66].

DA transport and inhibition assays. Uptake of DA by the transport active constructs of dDAT ($dDAT_{fc}$ and $dDAT_{mfc}$) used in this study was performed in HEK293S GnTI⁻ cells transfected with the cGFP fused dDAT constructs. Cells were transiently transfected with pEG-BacMam plasmid harboring the dDAT cGFP gene and incubated for 35–40 hrs at 37 °C with 5% CO_2 and 80% humidity. For the determination of inhibition potencies (IC_{50} values), transfected cells were resuspended in uptake assay buffer (25 mM HEPES-Tris pH 7.1, 130 mM NaCl, 5.4 mM KCl, 1.2 mM $CaCl_2$, 1.2 mM $MgSO_4$, 1 mM ascorbic acid, 5 mM glucose and 30 μM pargyline (Sigma Aldrich), a monoamine oxidase inhibitor) and incubated with varying concentrations of inhibitors at room temperature for 30 mins. This was followed by the addition of 2 μM of DA in a 1:100 molar ratio of [³H]-DA (Vitrax): [¹H]-DA (Sigma Aldrich) and incubated for 20 mins at room temperature. The transport activity was arrested with 0.5 ml of pre-chilled assay buffer containing 100 μM desipramine (Sigma Aldrich) added to each reaction. The cells were then washed twice with the same buffer before solubilizing them in 0.1 ml of 20 mM DDM for one hour at room temperature. Post-solubilization the material was subjected to centrifugation at $14,500 \times g$ for 30 mins to separate unsolubilized material. Following this, 0.1 ml of the supernatant was added to 0.5 ml of scintillation fluid (Ultima Gold, Perkin Elmer) and the radioactivity was estimated on MicroBeta scintillation counter (Perkin Elmer). Counts measured from cells incubated with 25 μM desipramine were considered as background. The background-subtracted, dose–response plots were analyzed using GraphPad Prism v.5.0.1 and K_i values were determined from Cheng–Prusoff's equation using the IC_{50} values obtained from the experiments.

For the determination of Michaelis–Menten constant (K_M), the $dDAT_{fc}$ transfected HEK293S GnTI⁻ cells were incubated with varying concentrations of DA (0.2 μM, 0.4 μM, 2 μM, 4 μM, 8 μM, 10 μM, and 20 μM) in 1:200 molar ratio of [³H]-DA:[¹H]-DA at room temperature in a 96-well plate. The uptake was arrested after 3 mins incubation at room temperature with 100 μM desipramine. The cells were washed twice with uptake buffer before solubilizing in 50 μl of 20 mM DDM. To this solubilized material 50 μl of scintillation fluid was added and the radioactivity was estimated on MicroBeta scintillation counter. The activity measured in untransfected cells was considered as background uptake. The background-subtracted initial uptake rates were plotted against above mentioned concentrations of DA to deduce the K_M value.

Binding and competition assays. Binding assays were performed with 20 nM of purified dDAT protein by scintillation proximity assay. For determining nisoxetine K_d, [³H] Nisoxetine (Perkin Elmer) (in 1:5 molar ratio) was used in the range of 0.1 nM to 500 nM with 100 μM desipramine added to the control samples. Competition assays were done with 50 nM [³H] Nisoxetine (in 1:5 molar ratio) with the concentration range for tramadol (Sigma Aldrich) being 100 nM to 3 mM, duloxetine (Sigma Aldrich) from 0.1 nM to 30 μM and milnacipran (Sigma Aldrich) from 1 nM to 100 μM. The assays were done in 1 mM DDM, 0.2 mM CHS, 20 mM Tris-Cl (pH 8), 300 mM NaCl and 5% glycerol. The background values were subtracted to plot the final curves in GraphPad prism v5.0.1 and the K_d values were calculated. The IC_{50} values obtained from binding competition assays were used to deduce the K_i values by Cheng–Prusoff's equation.

Statistical analysis. The biochemical assays performed were analyzed using GraphPad Prism v5.0.1. The significance tests were performed using two-sample t test assuming unequal variances in Microsoft Excel.

Reporting summary. Further information on research design is available in the Nature Research Reporting Summary linked to this article.

Data availability
Data supporting the findings of this manuscript are available from the corresponding author upon reasonable request. A reporting summary for this Article is available as a Supplementary Information file. The coordinates for the structures have been deposited in the Protein Data Bank with the following accession codes PDB6M0F, PDB6M0Z, PDB6M2R, PDB6M38, PDB6M3Z, PDB6M47. Source data are provided with this paper.

References
1. Kristensen, A. S. et al. SLC6 neurotransmitter transporters: structure, function, and regulation. *Pharm. Rev.* **63**, 585–640 (2011).
2. Focke, P. J., Wang, X. & Larsson, H. P. Neurotransmitter transporters: structure meets function. *Structure* **21**, 694–705 (2013).
3. Joseph, D., Pidathala, S., Mallela, A. K. & Penmatsa, A. Structure and gating dynamics of Na(+)/Cl(-) coupled neurotransmitter transporters. *Front. Mol. Biosci.* **6**, 80 (2019).
4. Vatner, S. F., Knight, D. R. & Hintze, T. H. Norepinephrine-induced beta 1-adrenergic peripheral vasodilation in conscious dogs. *Am. J. Physiol.* **249**, H49–H56 (1985).
5. Pertovaara, A. Noradrenergic pain modulation. *Prog. Neurobiol.* **80**, 53–83 (2006).
6. Atzori, M. et al. Locus ceruleus norepinephrine release: a central regulator of CNS spatio-temporal activation? *Front. Synaptic Neurosci.* **8**, 25 (2016).
7. Hurlemann, R. et al. Noradrenergic modulation of emotion-induced forgetting and remembering. *J. Neurosci.* **25**, 6343–6349 (2005).
8. Pignatelli, M. & Bonci, A. Role of dopamine neurons in reward and aversion: a synaptic plasticity perspective. *Neuron* **86**, 1145–1157 (2015).
9. Sara, S. J. The locus coeruleus and noradrenergic modulation of cognition. *Nat. Rev. Neurosci.* **10**, 211–223 (2009).
10. Von Euler, U. S. A specific sympathomimetic ergone in adrenergic nerve fibres (Sympathin) and its relations to adrenaline and nor-adrenaline. *Acta Physiol. Scand.* **12**, 73–97 (1946).
11. Ramos, B. P. & Arnsten, A. F. Adrenergic pharmacology and cognition: focus on the prefrontal cortex. *Pharm. Ther.* **113**, 523–536 (2007).
12. Torres, G. E., Gainetdinov, R. R. & Caron, M. G. Plasma membrane monoamine transporters: structure, regulation and function. *Nat. Rev. Neurosci.* **4**, 13–25 (2003).
13. Pacholczyk, T., Blakely, R. D. & Amara, S. G. Expression cloning of a cocaine- and antidepressant-sensitive human noradrenaline transporter. *Nature* **350**, 350–354 (1991).
14. Kilty, J. E., Lorang, D. & Amara, S. G. Cloning and expression of a cocaine-sensitive rat dopamine transporter. *Science* **254**, 578–579 (1991).
15. Blakely, R. D. et al. Cloning and expression of a functional serotonin transporter from rat brain. *Nature* **354**, 66–70 (1991).
16. Penmatsa, A., Wang, K. H. & Gouaux, E. X-ray structure of dopamine transporter elucidates antidepressant mechanism. *Nature* **503**, 85–90 (2013).
17. Coleman, J. A., Green, E. M. & Gouaux, E. X-ray structures and mechanism of the human serotonin transporter. *Nature* **532**, 334–339 (2016).
18. Coleman, J. A. et al. Serotonin transporter-ibogaine complexes illuminate mechanisms of inhibition and transport. *Nature* **569**, 141–145 (2019).
19. Giros, B. et al. Delineation of discrete domains for substrate, cocaine, and tricyclic antidepressant interactions using chimeric dopamine-norepinephrine transporters. *J. Biol. Chem.* **269**, 15985–15988 (1994).
20. Glowinski, J. & Axelrod, J. Inhibition of uptake of tritiated-noradrenaline in the intact rat brain by imipramine and structurally related compounds. *Nature* **204**, 1318–1319 (1964).
21. Giros, B., Jaber, M., Jones, S. R., Wightman, R. M. & Caron, M. G. Hyperlocomotion and indifference to cocaine and amphetamine in mice lacking the dopamine transporter. *Nature* **379**, 606–612 (1996).
22. Tatsumi, M., Groshan, K., Blakely, R. D. & Richelson, E. Pharmacological profile of antidepressants and related compounds at human monoamine transporters. *Eur. J. Pharm.* **340**, 249–258 (1997).
23. Iversen, L. Neurotransmitter transporters and their impact on the development of psychopharmacology. *Br. J. Pharm.* **147**, S82–S88 (2006).

24. Ashburn, T. T. & Thor, K. B. Drug repositioning: identifying and developing new uses for existing drugs. *Nat. Rev. Drug Discov.* **3**, 673–683 (2004).

25. Apparsundaram, S., Stockdale, D. J., Henningsen, R. A., Milla, M. E. & Martin, R. S. Antidepressants targeting the serotonin reuptake transporter act via a competitive mechanism. *J. Pharm. Exp. Ther.* **327**, 982–990 (2008).

26. Wang, K. H., Penmatsa, A. & Gouaux, E. Neurotransmitter and psychostimulant recognition by the dopamine transporter. *Nature* **521**, 322–327 (2015).

27. Plenge, P. et al. Steric hindrance mutagenesis in the conserved extracellular vestibule impedes allosteric binding of antidepressants to the serotonin transporter. *J. Biol. Chem.* **287**, 39316–39326 (2012).

28. Singh, S. K., Piscitelli, C. L., Yamashita, A. & Gouaux, E. A competitive inhibitor traps LeuT in an open-to-out conformation. *Science* **322**, 1655–1661 (2008).

29. Quick, M. et al. Binding of an octylglucoside detergent molecule in the second substrate (S2) site of LeuT establishes an inhibitor-bound conformation. *Proc. Natl Acad. Sci. USA* **106**, 5563–5568 (2009).

30. Janowsky, A., Tosh, D. K., Eshleman, A. J. & Jacobson, K. A. Rigid adenine nucleoside derivatives as novel modulators of the human sodium symporters for dopamine and norepinephrine. *J. Pharm. Exp. Ther.* **357**, 24–35 (2016).

31. Mostyn, S. N. et al. Identification of an allosteric binding site on the human glycine transporter, GlyT2, for bioactive lipid analgesics. *Elife* **8**, e47150(2019).

32. Sorensen, L. et al. Interaction of antidepressants with the serotonin and norepinephrine transporters: mutational studies of the S1 substrate binding pocket. *J. Biol. Chem.* **287**, 43694–43707 (2012).

33. Wang, H. et al. Structural basis for action by diverse antidepressants on biogenic amine transporters. *Nature* **503**, 141–145 (2013).

34. Porzgen, P., Park, S. K., Hirsh, J., Sonders, M. S. & Amara, S. G. The antidepressant-sensitive dopamine transporter in *Drosophila melanogaster*: a primordial carrier for catecholamines. *Mol. Pharm.* **59**, 83–95 (2001).

35. Penmatsa, A., Wang, K. H. & Gouaux, E. X-ray structures of *Drosophila* dopamine transporter in complex with nisoxetine and reboxetine. *Nat. Struct. Mol. Biol.* **22**, 506–508 (2015).

36. Paczkowski, F. A., Sharpe, I. A., Dutertre, S. & Lewis, R. J. chi-Conotoxin and tricyclic antidepressant interactions at the norepinephrine transporter define a new transporter model. *J. Biol. Chem.* **282**, 17837–17844 (2007).

37. Claxton, D. P. et al. Ion/substrate-dependent conformational dynamics of a bacterial homolog of neurotransmitter:sodium symporters. *Nat. Struct. Mol. Biol.* **17**, 822–829 (2010).

38. Krishnamurthy, H. & Gouaux, E. X-ray structures of LeuT in substrate-free outward-open and apo inward-open states. *Nature* **481**, 469–474 (2012).

39. Zhang, Y. W. et al. Structural elements required for coupling ion and substrate transport in the neurotransmitter transporter homolog LeuT. *Proc. Natl Acad. Sci. USA* **115**, E8854–E8862 (2018).

40. Moller, I. R. et al. Conformational dynamics of the human serotonin transporter during substrate and drug binding. *Nat. Commun.* **10**, 1687 (2019).

41. Nielsen, A. K. et al. Substrate-induced conformational dynamics of the dopamine transporter. *Nat. Commun.* **10**, 2714 (2019).

42. Cheng, M. H. & Bahar, I. Monoamine transporters: structure, intrinsic dynamics and allosteric regulation. *Nat. Struct. Mol. Biol.* **26**, 545–556 (2019).

43. Moron, J. A., Brockington, A., Wise, R. A., Rocha, B. A. & Hope, B. T. Dopamine uptake through the norepinephrine transporter in brain regions with low levels of the dopamine transporter: evidence from knock-out mouse lines. *J. Neurosci.* **22**, 389–395 (2002).

44. Koldso, H., Christiansen, A. B., Sinning, S. & Schiott, B. Comparative modeling of the human monoamine transporters: similarities in substrate binding. *ACS Chem. Neurosci.* **4**, 295–309 (2013).

45. Schlessinger, A. et al. Structure-based discovery of prescription drugs that interact with the norepinephrine transporter, NET. *Proc. Natl Acad. Sci. USA* **108**, 15810–15815 (2011).

46. Focht, D. et al. A non-helical region in transmembrane helix 6 of hydrophobic amino acid transporter MhsT mediates substrate recognition. *EMBO J.* **40**, e105164 (2021).

47. Nagy, P. I., Alagona, G., Ghio, C. & Takacs-Novak, K. Theoretical conformational analysis for neurotransmitters in the gas phase and in aqueous solution. Norepinephrine. *J. Am. Chem. Soc.* **125**, 2770–2785 (2003).

48. Nagy, P. I., Alagona, G. & Ghio, C. Theoretical studies on the conformation of protonated dopamine in the gas phase and in aqueous solution. *J. Am. Chem. Soc.* **121**, 8226–8231 (1999).

49. Du, X. et al. Insights into protein-ligand interactions: mechanisms, models, and methods. *Int. J. Mol. Sci.* **17**,144 (2016).

50. Arnold, L. M., Crofford, L. J., Martin, S. A., Young, J. P. & Sharma, U. The effect of anxiety and depression on improvements in pain in a randomized, controlled trial of pregabalin for treatment of fibromyalgia. *Pain. Med.* **8**, 633–638 (2007).

51. Coleman, J. A. & Gouaux, E. Structural basis for recognition of diverse antidepressants by the human serotonin transporter. *Nat. Struct. Mol. Biol.* **25**, 170–175 (2018).

52. Hoepping, A., Johnson, K. M., George, C., Flippen-Anderson, J. & Kozikowski, A. P. Novel conformationally constrained tropane analogues by 6-endo-trig radical cyclization and stille coupling - switch of activity toward the serotonin and/or norepinephrine transporter. *J. Med. Chem.* **43**, 2064–2071 (2000).

53. Andersen, J., Kristensen, A. S., Bang-Andersen, B. & Stromgaard, K. Recent advances in the understanding of the interaction of antidepressant drugs with serotonin and norepinephrine transporters. *Chem. Commun.* **7**, 3677–3692 (2009).

54. Grond, S. & Sablotzki, A. Clinical pharmacology of tramadol. *Clin. Pharmacokinet.* **43**, 879–923 (2004).

55. Dayer, P., Desmeules, J. & Collart, L. [Pharmacology of tramadol]. *Drugs* **53**, 18–24 (1997).

56. Rickli, A., Liakoni, E., Hoener, M. C. & Liechti, M. E. Opioid-induced inhibition of the human 5-HT and noradrenaline transporters in vitro: link to clinical reports of serotonin syndrome. *Br. J. Pharm.* **175**, 532–543 (2018).

57. Andersen, J. et al. Molecular determinants for selective recognition of antidepressants in the human serotonin and norepinephrine transporters. *Proc. Natl Acad. Sci. USA* **108**, 12137–12142 (2011).

58. Andersen, J., Ringsted, K. B., Bang-Andersen, B., Stromgaard, K. & Kristensen, A. S. Binding site residues control inhibitor selectivity in the human norepinephrine transporter but not in the human dopamine transporter. *Sci. Rep.* **5**, 15650 (2015).

59. Chen, C. et al. Studies on the SAR and pharmacophore of milnacipran derivatives as monoamine transporter inhibitors. *Bioorg. Med. Chem. Lett.* **18**, 1346–1349 (2008).

60. Goehring, A. et al. Screening and large-scale expression of membrane proteins in mammalian cells for structural studies. *Nat. Protoc.* **9**, 2574–2585 (2014).

61. Kabsch, W. XDS. *Acta Crystallogr D. Biol. Crystallogr* **66**, 125–132 (2010).

62. Winn, M. D. et al. Overview of the CCP4 suite and current developments. *Acta Crystallogr. D. Biol. Crystallogr* **67**, 235–242 (2011).

63. McCoy, A. J. et al. Phaser crystallographic software. *J. Appl. Crystallogr.* **40**, 658–674 (2007).

64. Zwart, P. H. et al. Automated structure solution with the PHENIX suite. *Methods Mol. Biol.* **426**, 419–435 (2008).

65. Emsley, P. & Cowtan, K. Coot: model-building tools for molecular graphics. *Acta Crystallogr. D. Biol. Crystallogr.* **60**, 2126–2132 (2004).

66. Afonine, P. V. et al. FEM: feature-enhanced map. *Acta Crystallogr. D. Biol. Crystallogr.* **71**, 646–666 (2015).

Author contributions

S.P. performed protein expression, purification, crystallization, and uptake measurements. A.K.M. developed the methodology for heterologous expression of the antibody fragment and performed biochemical assays involving binding. D.J. performed biochemical analysis and aided in the preparation of figures. A.P. designed the study and performed crystallographic analyses. A.P. wrote the manuscript with inputs from all the authors.

Competing interests

The authors declare no competing interests.

Additional information

Supplementary information The online version contains supplementary material available at https://doi.org/10.1038/s41467-021-22385-9.

Correspondence and requests for materials should be addressed to A.P.

Peer review information *Nature Communications* thanks Jeff Abramson, Claus Loland, and the other, anonymous, reviewer(s) for their contribution to the peer review of this work. Peer reviewer reports are available.

Reprints and permission information is available at http://www.nature.com/reprints

Publisher's note Springer Nature remains neutral with regard to jurisdictional claims in published maps and institutional affiliations.

Structural insights into GABA transport inhibition using an engineered neurotransmitter transporter

Deepthi Joseph , Smruti Ranjan Nayak & Aravind Penmatsa*

Abstract

γ-aminobutyric acid (GABA) is the major inhibitory neurotransmitter, and its levels in the synaptic space are controlled by the GABA transporter isoforms (GATs). GATs are structurally related to biogenic amine transporters but display interactions with distinct inhibitors used as anti-epileptics. In this study, we engineer the binding pocket of *Drosophila melanogaster* dopamine transporter to resemble GAT1 and determine high-resolution X-ray structures of the modified transporter in the substrate-free state and in complex with GAT1 inhibitors NO711 and SKF89976a that are analogs of tiagabine, a medication prescribed for the treatment of partial seizures. We observe that the primary binding site undergoes substantial shifts in subsite architecture in the modified transporter to accommodate the two GAT1 inhibitors. We also observe that SKF89976a additionally interacts at an allosteric site in the extracellular vestibule, yielding an occluded conformation. Interchanging SKF89976a interacting residue in the extracellular loop 4 between GAT1 and dDAT suggests a role for this motif in the selective control of neurotransmitter uptake. Our findings, therefore, provide vital insights into the organizational principles dictating GAT1 activity and inhibition.

Introduction

The levels of the major inhibitory neurotransmitter, γ-aminobutyric acid (GABA), are controlled by the activity of GABA transporters (GATs) in the presynaptic and glial cell membranes (Florey & Mc, 1959; Iversen & Neal, 1968). Multiple isoforms of GAT mediate the Na^+/Cl^--dependent uptake of GABA in neurons, glia, and other cell types (Scimemi, 2014). Exocytic release of GABA in the synapse mediates the generation of inhibitory postsynaptic currents (IPSCs)

mediated through the ionotropic $GABA_A$ receptors and metabotropic $GABA_B$ receptors in the postsynaptic neurons (Krnjević & Schwartz, 1967; Bettler *et al*, 2004; Jacob *et al*, 2008). GABA is primarily responsible for synchronizing activity among neuronal networks and balances the excitatory neurotransmission mediated by glutamate (Owens & Kriegstein, 2002; Khazipov, 2016). Consequently, impaired GABAergic signaling leads to hypersynchronous excitatory discharges that cause epileptic conditions (Treiman, 2001; Khazipov, 2016). Therefore, control of GABA levels and GABA receptor activation forms a therapeutic basis to alleviate epileptic disorders (Treiman, 2001; Sperk *et al*, 2004). Besides neuronal roles, GABA is also vital for affecting neural development (Ben-Ari, 2002), modulation of gastrointestinal function (Hyland & Cryan, 2010), immunomodulation of inflammatory responses (Bhat *et al*, 2010), and regulation of cardiovascular activity (Bentzen & Grunnet, 2011).

Restoring GABA levels in the neural synapse is possible by inhibiting GABA uptake activity mediated through GAT isoforms (GATs 1, 2, 3 and BGT1; Latka *et al*, 2020a, Zhou & Danbolt, 2013). Early studies of GABA transport involved the identification of high-affinity uptake of radiolabeled GABA into slices of rat brain cortex by Iversen and Neal followed by the cloning of rat GAT1 by Kanner *et al* (Iversen & Neal, 1968; Guastella *et al*, 1990). GAT1 and GAT3 are the primary neuronal isoforms of the GABA transporter that transports one molecule of GABA in combination with $2Na^+$ and $1Cl^-$ ions resulting in the electrogenic movement of GABA across the synaptic membrane (Kavanaugh *et al*, 1992; Hilgemann & Lu, 1999; Lu & Hilgemann, 1999). Substrate analogs like β-alanine, cis-3-aminocyclohexanecarboxylicacid (ACHC), nipecotic acid, and guvacine can compete with GABA for uptake (Krogsgaard-Larsen, 1980; Dalby, 2003). Nipecotic acid and guvacine serve as templates for attaching branched aromatic groups to synthesize competitive inhibitors of GAT activity and facilitate movement across the blood–brain barrier (Ali *et al*, 1985; Borden *et al*, 1994; Soudijn & van Wijngaarden, 2000). Among the specific inhibitors of GAT1 activity, tiagabine (Gabitril) is prescribed as medication to treat partial seizures (Suzdak & Jansen, 1995). Analogs of tiagabine, NO711, and SKF89976a are also potent inhibitors of GAT1 mediated uptake and are known to mediate competitive inhibition of GAT activity (Clausen *et al*, 2006; Zafar & Jabeen, 2018; Latka *et al*, 2020a).

GATs are structurally related to the biogenic amine and glycine transporters of the solute carrier 6 family (Kristensen *et al*, 2011). Despite being the first SLC6 member to be cloned and characterized

Molecular Biophysics Unit, Indian Institute of Science, Bangalore, India
*Corresponding author. Tel: +91 8022932458; E-mail: penmatsa@iisc.ac.in

(SLC6A1), the high-resolution structure of a GAT isoform remains elusive. All members of the solute carrier 6 family are composed of 12 transmembrane (TM) helices that comprise symmetrically organized, discontinuous TMs 1a, 1b and 6a, 6b that gate the substrate and ion transport through alternating access (Joseph *et al*, 2019). Despite having high sequence and structural similarities with SLC6 members involved in biogenic amine and glycine transport, GATs have distinct substrate recognition propensities and inhibitor binding characteristics. In this context, specific inhibitors of GABA uptake like tiagabine, NO711, and SKF89976a have distinct chemical structures and display no interactions with the biogenic amine transporters that are inhibited with high inhibitory potency by antidepressants and psychostimulants.

Recent structural studies on the *Drosophila melanogaster* dopamine transporter (dDAT), the human serotonin transporter (hSERT), and the human glycine transporter 1 (hGlyT1) have revealed mechanistic aspects of substrate transport and transport inhibition by inhibitors interacting at the orthosteric and allosteric sites (Penmatsa *et al*, 2013; Coleman *et al*, 2016; Shahsavar *et al*, 2021). In particular, the dDAT has proven to be a versatile model to study interactions of catecholamine neurotransmitters, tricyclic antidepressants, psychostimulants, and chronic pain inhibitors at a high resolution due to the availability of thermostabilizing mutants that render the transporter highly stable and an antibody fragment available for use as a crystallization chaperone (Penmatsa *et al*, 2013; Wang *et al*, 2015; Pidathala *et al*, 2021).

In this study, we attempt to understand the fundamental discrepancies between GABA and catecholamine transporter inhibition through engineering the residues of GAT1 orthosteric site into the primary binding site of a thermostabilized dDAT. In doing so, we observe that the engineered construct of dDAT (dDAT$_{GAT}$) interacts with specific inhibitors of GATs including NO711 and SKF89976a, although it lacks GABA transport activity. The high-resolution X-ray structures of dDAT$_{GAT}$ in complex with NO711 and SKF89976a display a reorganized subsite architecture in the primary binding site that reveals the basis for altered inhibitor interaction propensities between GATs and biogenic amine transporters. We further observe an allosteric binding site for SKF89976a in the extracellular vestibule that provides a rationale for its ability to display both competitive and noncompetitive interactions in GATs (Krause & Schwarz, 2005). Using the GAT1 from *Rattus norvegicus* (GAT1$_{WT}$) for biochemical analysis, we validate the structural findings we observe in dDAT$_{GAT}$ and additionally characterize the importance of the extracellular loop 4 (EL4) in affecting selective substrate entry across SLC6 neurotransmitter transporters.

Results

Engineering GAT1 primary binding site into dDAT

The solute carrier 6 family transporters share a similar architecture but display distinct substrate specificities depending on the nature of the cognate neurotransmitter being transported by the neurotransmitter transporters. Despite high structural similarity, the catecholamine neurotransmitter transporters, dDAT, hDAT, and hNET, share a sequence identity in the range of 41–46% with GAT and GlyT isoforms (Fig EV1). Substrate recognition and competitive

inhibitor interactions in neurotransmitter sodium symporters (NSS) occur at the primary binding site where a bulk of the residue differences between the transporters lie. Based on an alignment of the crystallized construct of dDAT with hGAT1 homology model generated using I-TASSER, we analyzed residues within a 10 Å radius of the primary binding site and facing the binding pocket of dDAT. A similar strategy was successfully employed previously using LeuBAT to understand the interactions of selective serotonin reuptake inhibitors (SSRIs; Wang *et al*, 2013). The equivalent residues of hGAT1 were substituted in a partly thermostabilized (ts) yet functional construct of dDAT (ts2-L415A, V74A; Wang *et al*, 2015). The substitutions include the residues F43Y and D46G around subsite A (Tyr60 and Gly63 in GAT1, respectively), V120L, D121N, S422Q, G425T, and S426V in subsite B (Leu136, Asn137, Gln397, Thr400, and Val401 in GAT1) and A117S, F325L, and V327S in subsite C (Ser133, Leu300, and Ser302 in GAT1; Figs EV2 and 1A). In addition to the primary binding site mutations, an additional mutation was made in the extracellular vestibule in EL4 (E384S). The mutations were carried out progressively and analyzed for homogeneity and expression level using fluorescence-detection size-exclusion chromatography (FSEC; Appendix Table S1 and Fig S1A–H). While some construct combinations suffered from poor expression and lack of homogeneity, the final construct carrying 11 mutations (dDAT$_{GAT}$) yielded a homogenous FSEC profile (Appendix Table S1 and Fig S1H). Despite a homogenous FSEC profile, the ts2 dDAT$_{GAT}$ was observed to yield a large fraction of aggregated protein upon large-scale purification that was not amenable for crystallization trials (Appendix Fig S2A). We, therefore, included three additional stabilizing mutations into dDAT (V275A, V311A, and G538L), carrying GAT1-like mutations (Penmatsa *et al*, 2013). The purification of ts5 dDAT$_{GAT}$ construct yielded improved levels of homogenous protein (Appendix Fig S2B) although, as known from earlier studies with thermostabilized dDAT, the transporter is locked into the outward-open conformation and does not retain any transport activity (Appendix Fig S2C; Penmatsa *et al*, 2013).

The purified dDAT$_{GAT}$ in detergent micelles displays weak interactions with the GAT1 inhibitors NO711 and SKF89976a with a K_d value of 10 and 34 μM using microscale thermophoresis measurements, respectively (Fig 1B–F). Interactions of substrates like GABA and nipecotic acid with dDAT$_{GAT}$ did not yield a clear binding signal likely due to weaker affinity of substrates to dDAT$_{GAT}$ in comparison with GAT1. Since the observed binding affinities for ts5 dDAT$_{GAT}$ were weaker than the GABA transport inhibition potencies reported for GAT1, we employed the GAT1$_{WT}$ to observe and validate our structural findings with dDAT$_{GAT}$. The GAT1$_{WT}$ displayed GABA transport activity in HEK293S (GnTI⁻) cells with K_M value of 11 μM and inhibition constant toward nipecotic acid at a value of 14 μM (Fig 1G and H). Similarly, inhibitors of GABA uptake like tiagabine, NO711, and SKF89976a (Fig 1B) had inhibition potencies of 0.72, 1.0, and 7 μM, respectively (Fig 1I and Appendix Table S2). The subsequent structural studies in the manuscript have been carried out using ts5 dDAT$_{GAT}$, referred to henceforth as dDAT$_{GAT}$, in complex with a heterologously expressed fragment-antigen binding (Fab 9D5) that is essential for crystallizing the diverse constructs of dDAT. The interactions of the Fab are at the cytosolic face of dDAT and do not interfere with the inhibitor interactions with the transporter (Penmatsa *et al*, 2013, Pidathala *et al*, 2021; Appendix Fig S2D).
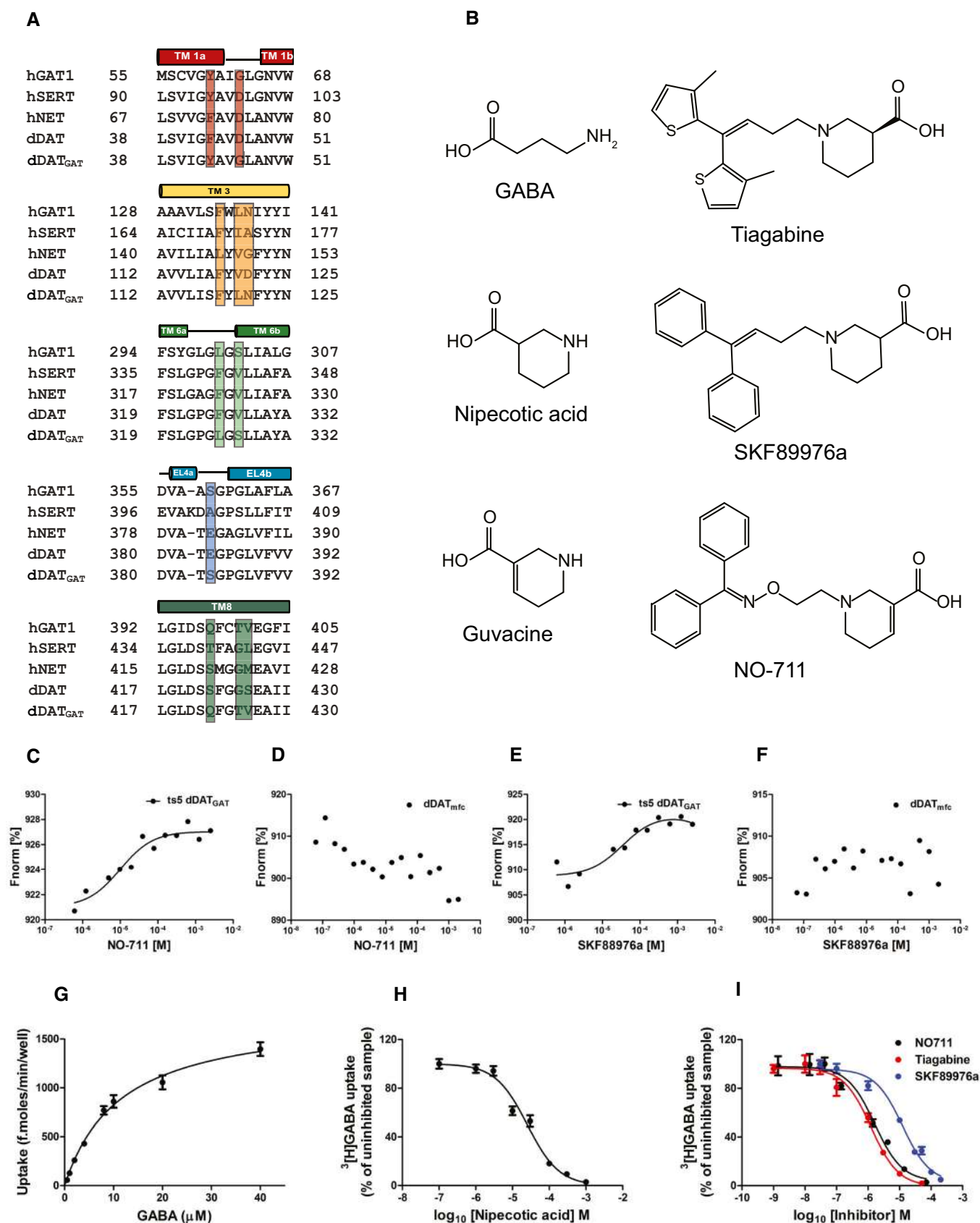
Figure 1.

**Figure 1. Engineering a GAT1 binding site into dDAT.**

A   Sequence alignment between hGAT1, hSERT, hNET, dDAT, and dDAT$_{GAT}$ in the vicinity of the primary binding site. GAT1-like substitutions (11 mutations) were carried out in dDAT.

B   Chemical structures of GABA and substrate analogs, nipecotic acid and guvacine. Structures of specific inhibitors of GAT1 tiagabine, NO711, and SKF89976a.

C   Microscale thermophoresis (MST) with purified ts5 dDAT$_{GAT}$ construct displaying affinity of 10 μM for NO711.

D   dDAT$_{mfc}$ did not show any interactions with NO711 in the MST experiments.

E   SKF89976a interacts with purified ts5 dDAT$_{GAT}$ construct with an affinity of 34 μM.

F   MST experiments display no interactions of purified dDAT$_{mfc}$ with SKF89976a. The MST profiles shown are one of two independent measurements.

G   Michaelis–Menten uptake kinetics of ^{3}H-GABA by the GAT1$_{WT}$ used in the study displaying a K_M value of 11.4 μM.

H   Inhibition of ^{3}H-GABA uptake by the substrate analog nipecotic acid displaying a K_i value of 14.4 μM.

I   Inhibition of ^{3}H-GABA uptake through GAT1$_{WT}$ by tiagabine (K_i = 725 nM), NO711 (1.07 μM) and SKF89976a (7.3 μM).

Data information: All measurements of inhibition potency were the result of two independent experiments performed in triplicate (n = 6), and all the points were used for calculating the values where the error bars represent s.e.m. Control data are included in Appendix Figs S6 and S7.

Source data are available online for this figure.

Substrate-free dDAT$_{GAT}$ structure reveals altered subsite distribution

The structure of the substrate-free dDAT$_{GAT}$ construct was determined to a resolution of 3.2 Å in outward-open conformation with clear densities being visible for all the side chains including the substituted residues (Figs 2A and EV3A). The primary binding site

and the extracellular vestibule leading into it were filled with weak densities into which water molecules were modeled (Fig EV3B). A comparison of the substrate-free structures of the dDAT$_{GAT}$ and dDAT$_{NET}$ constructs display a Cα rmsd of 0.5 Å indicating relatively unaltered main chain conformation between the two structures. Structural changes in the main chain are primarily confined to the substrate/inhibitor binding site, particularly in the region of the
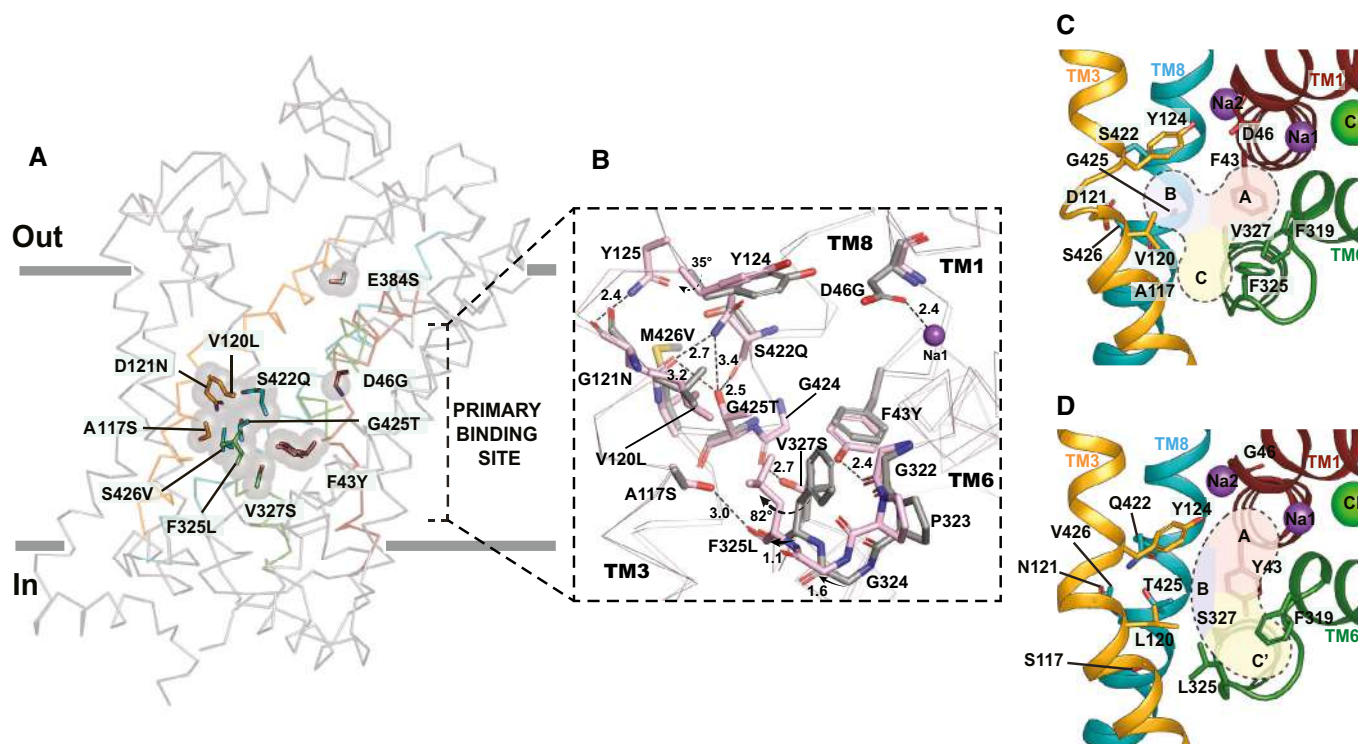
Figure 2. Substrate-free structure of dDAT$_{GAT}$ displays an altered subsite organization.

A   X-ray structure of the substrate-free dDAT$_{GAT}$ (PDB id. 7WGD) displayed with substitutions made within the primary binding site in TMs 1 (deep red), 3 (orange), 6 (green), and 8 (cyan). An additional mutation (E384S) was carried out in the vestibule with a total of 11 substitutions in dDAT to engineer the dDAT$_{GAT}$.

B   Panel displays an overlay of the substrate-free structures of dDAT (PDB id. 6M0F) (gray) and dDAT$_{GAT}$ (PDB id. 7WGD) (light pink) with a Cα rmsd of 0.50 Å. Altered position of the residues along with the angular shifts and displacement of the main chain are depicted. H-bond networks resulting out of the substitutions within the binding pocket are displayed as dashed lines.

C   Conventional trilobed subsite architecture observed in biogenic amine neurotransmitter transporters.

D   Altered subsite architecture displayed with the creation of a new subsite C′ with a substantially minimized subsite B accessible to GAT1 inhibitors resulting from the GAT1-like substitutions.

TM6 linker (Fig 2B). Substitution of multiple residues in the binding site causes substantial changes to the side chain H-bonding network that affects the organization of the inhibitor binding site. For instance, in subsite A, a conserved aspartate in TM1b (Asp46^{dDAT}) in all biogenic amine transporters (Fig 2C) is substituted to a glycine in GATs (Gly63^{GAT1}), GlyTs (Gly119^{GlyT1}) and the bacterial amino acid transporter LeuT (Gly24^{LeuT}). The glycine substitution accommodates the carboxylate group of the substrates that participates in the coordination of Na$^+$ ion at site 1, as observed in LeuT (Yamashita *et al*, 2005). Subsite B, lined by residues in TM3 and TM8, forms a partially hydrophobic cavity in the case of the DAT, NET, and SERT. The GAT1-like substitutions in this region, D121N, S422Q, G425T, and S426V occlude this subsite through side chain interactions mediated by a network of H-bonds. In dDAT$_{GAT}$, the interactions are between side chain amide groups of Asn121 and Gln422 (2.7 Å), main chain carbonyl of Gln422 (C=O) with γ-hydroxyl group of Thr425 (2.5 Å), Asn121 γ-amide group with γ-hydroxyl group of Thr425 (3.2 Å) and between the main chain of Asn121 (C=O) and side chain of Asn125 (2.4 Å). These interactions substantially minimize the accessible cavity of subsite B in dDAT$_{GAT}$, which is a critical region that aids in enhancing the affinities of inhibitors of catecholamine transporters. Major changes in the organization of subsite C are also observed wherein GAT1-like substitutions alter the position of the TM6 linker (Fig 2D). In earlier studies, we observed the presence of subsite C interactions in a gap between TM6 linker and TM3 that allows inhibitors to have specific interactions, particularly in the case of the norepinephrine transporter (NET; Pidathala *et al*, 2021). In dDAT$_{GAT}$ construct, this cavity is blocked due to the widening of the TM6 linker, which is the site of F325L substitution. In the substrate-free structure of dDAT (PDB.id 6M0F), the disordered TM6 linker comprising residues Gly322-Pro323-Gly324 is held in place at a distance of 3.9 Å between the main chain carbonyl of Gly322 (ith residue) and main chain amide of Phe325 (i + 3 residue; Cα-Cα distance 6.0 Å). In the dDAT$_{GAT}$, this motif is widened with a corresponding distance between main chain carbonyl of Gly322 and amide (-NH-) group of Leu325 being 4.8 Å (Cα-Cα distance 6.8 Å). This likely occurs in case of dDAT$_{GAT}$ due to the introduction of H-bond interactions between the Gly322 carbonyl with the hydroxyl group of F43Y substitution and the position of Leu325 shifting further by 1.1 Å due to a new H-bond interaction of the Leu325 carbonyl group with the side chain hydroxyl group of Ser117 substitution in dDAT$_{GAT}$ (Fig 2B). These interactions block access to subsite C and open up an alternate subsite within the widened TM6 linker that we refer to as the subsite C′ (Fig 2D). The altered subsite architecture displayed in the engineered dDAT$_{GAT}$ substrate-free structure can, therefore, underlie the discrete inhibitor specificities observed in the GATs in comparison with biogenic amine transporters.

NO711 and SKF89976a interact with the engineered primary binding site

In order to analyze the interactions of GAT1-specific inhibitors with the engineered dDAT$_{GAT}$ construct, we crystallized dDAT$_{GAT}$ in complex with NO711 and SKF89976a. The X-ray structures of the inhibitor-bound complexes were determined to a resolution of 2.75 and 2.9 Å, respectively (Appendix Table S3). Both inhibitors are analogs of tiagabine and are known to inhibit GABA uptake

specifically in GAT1 isoform, with high affinity (Borden *et al*, 1994). NO711 is a derivative of guvacine and has a diphenylmethylene group that is linked with a 2-amino oxyethyl group to the guvacine moiety (Fig 1B). The NO711-bound complex displays an outward-open state that is typical of most dDAT structures. The density for NO711 could be clearly identified in the primary binding site with the guvacine moiety interacting close to subsite A (Appendix Fig S3A, and Fig 3A and B). The carboxylate group of guvacine occupies the pocket that is created due to the substitution of D46G and participates in the coordination of the Na$^+$ ion (3.1 Å) and also interacts with the hydroxyl group of Tyr124 at a distance of 2.9 Å, which is conserved in GAT1 (Tyr140), through a H-bond. Tyr140 of GAT1 was also implicated in neurotransmitter recognition and substitution at this position, Y140F, led to impaired recognition of GABA (Bismuth *et al*, 1997), likely due to the interactions that the hydroxyl group could have with the carboxylate of the substrate. The interaction with the inhibitor shifts the Cα-Cβ dihedral angle of Tyr124 by 34° in comparison with the substrate-free dDAT$_{GAT}$, where it displays water-mediated interactions with the side chain of Asp475 (TM10). The linker connecting the guvacine with the diphenyl methylene group is in a bent configuration in the binding pocket and accommodates the two aromatic groups away from subsites B and C (Fig 3A and B). The phenyl group that is above the plane of the inhibitor interacts with edge-to-face aromatic interactions with Phe319 that could stabilize the outward-open state in GAT1 (Fig 3A). Alternately and rather interestingly, the second phenyl group is wedged inside the cavity created by the widening of the TM6 linker in the newly observed subsite C′ (Fig 3A). The phenyl group of NO711 forms a network of aromatic and hydrophobic interactions with Phe318, Phe319, and a displaced Leu325 (F325L equivalent to Leu300^{GAT1}). The displacement of the Leu325 in TM6 linker is clearly a prerequisite for NO711 to bind since the Phe325 in the substrate-free and nisoxetine-bound structures of dDAT (PDB.ids 6M0F, 4XNU) would clearly clash with the phenyl group of NO711 and requires displacement for the inhibitor to interact with subsite C′ in TM6 linker region (Fig 3F). The Leu325 is displaced by about 1.3 Å at its Cα position and undergoes a ~70° rotameric shift in the Cα-Cβ torsion angle to facilitate inhibitor interactions and avoid clashes with the aryl groups of the inhibitors (Fig 3F).

The structure of the SKF89976a complexed to dDAT$_{GAT}$ was resolved to a resolution of 2.9 Å that also revealed clear density for the inhibitor bound in the primary binding site (Fig 3C and D; Appendix Fig S3B). In addition to the inhibitor bound in the binding site, an additional density for SKF89976a was observed in the extracellular vestibule (discussed later). SKF89976a is a nipecotic acid derivative, and the inhibitor pose overlaps nearly exactly with that of NO711 except for linker region of the two drugs where NO711 has an additional atom compared with SKF89976a (Fig 3E). The nipecotic acid moiety closely interacts in the vicinity of subsite A displaying coordination of Na$^+$ bound at site 1 (3.6 Å) and a H-bond interaction with Tyr124 hydroxyl group (3.4 Å; Fig 3C). The diphenyl butylene moiety of SKF89976a is surrounded by similar groups in subsite C′ and lacks any interactions in the subsite B, and just like the NO711-bound structure, the Leu325 is displaced by a torsional angle shift of ~85°. However, unlike the NO711-bound dDAT$_{GAT}$, the position of Phe319 in the SKF89976a-bound dDAT$_{GAT}$ is in an occluded state with Phe319 shifting by ~100° in the Cα-Cβ
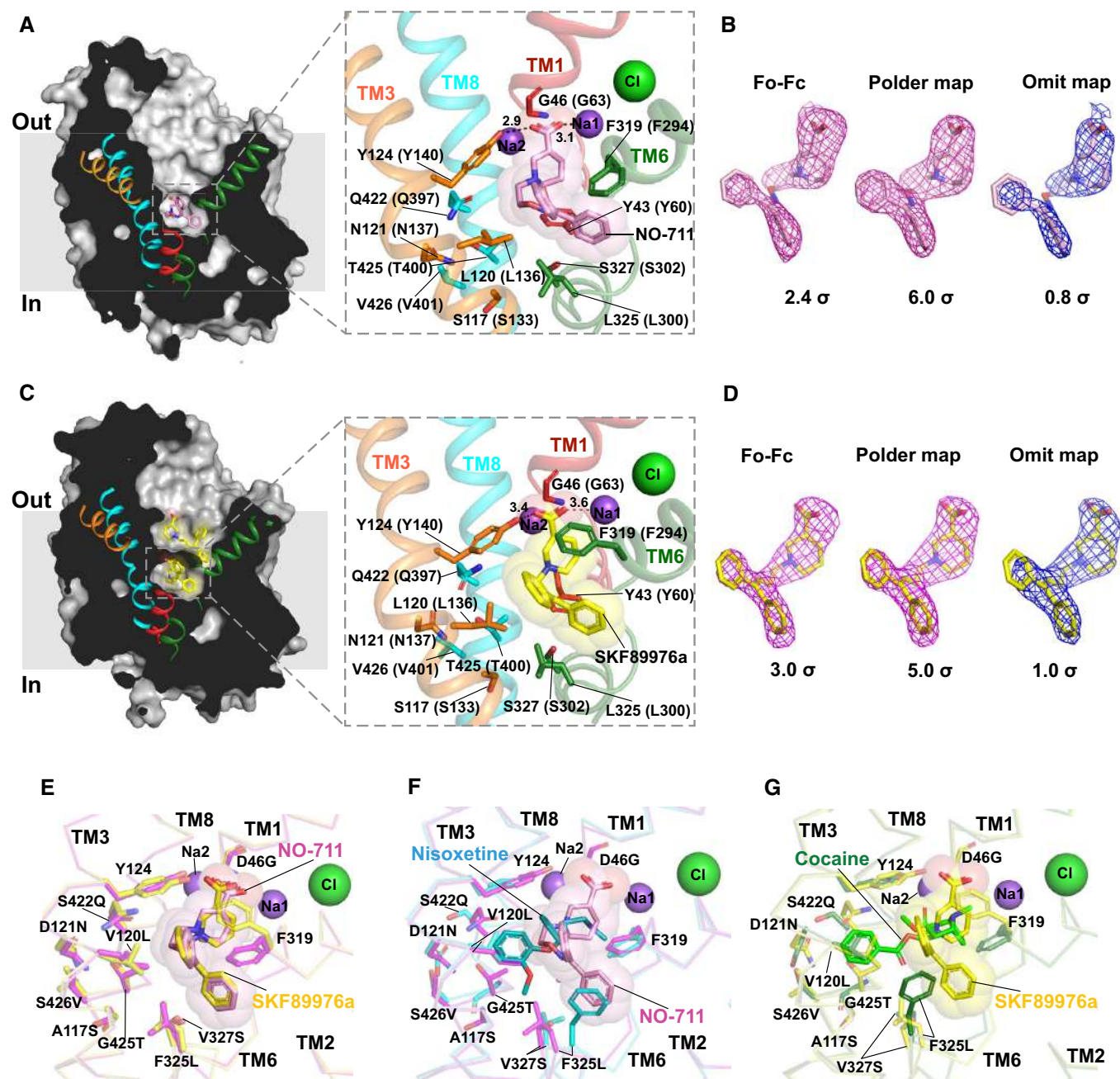
Figure 3. Interactions of competitive inhibitors NO711 and SKF89976a in the primary binding site.

A Sagittal section of the X-ray structure of the dDAT$_{GAT}$ in complex with the drug NO711 displays interactions of the guvacine moiety accommodated within subsite A with the carboxylate group displaying interactions with the Na at site 1. The diaryl group attached to guvacine with a long linker interacts within the TM6 linker to form aromatic π stacking interactions with the F319 and plausible CH-π interactions L325.

B Fo-Fc (2.4σ), Polder (6.0σ) and composite omit maps (0.8σ) of the NO711 interacting in the primary binding site of dDAT$_{GAT}$.

C X-ray structure surface cutaway (sagittal section) displaying interactions of SKF89976a in the primary binding site and allosteric site. The molecule interacts with a very similar pose as that of NO711. The F319 is, however, in an occluded state unlike the NO711-bound dDAT$_{GAT}$.

D Fo-Fc (3.0σ), Polder map (5.0σ) and composite omit map (1.0σ) of SKF89976a bound in the primary binding site.

E Structural overlaps of NO711 and SKF89976a-bound dDAT$_{GAT}$ display very similar binding pose of the two drugs; Cα rmsd of 0.37 Å.

F Structural comparison of nisoxetine-bound dDAT (PDB id. 4XNU) and NO711-bound dDAT$_{GAT}$.

G Structural comparison of cocaine-bound dDAT (PDB id. 4XP4) and SKF89976a-bound dDAT$_{GAT}$.

torsion angle to form an occluded state of the transporter (Fig 3E) that resembles the occluded state of a dichlorophenylethylamine-bound dDAT (PDB.id 4XPA; Appendix Fig S4). A comparison of the

SKF89976a complexed dDAT$_{GAT}$ structure with cocaine-bound dDAT (PDB.id 4XP4) reveals clashes of the cocaine's benzoyl ester moiety with the GAT1-like substitutions around subsite B region

with G425T, D121N and S422Q that interact among themselves with H-bonds. The G425T side chain sterically prevents the interaction of any hydrophobic moiety of the inhibitor at subsite B (Fig 3G). While multiple docking and simulation studies done with inhibitors, interacting with GAT1, display guvacine and nipecotic acid interactions close to subsite A interacting with Na1 and Tyr140^{GAT1}, the diaryl groups of tiagabine are predicted to dock within the vestibule (Skovstrup *et al*, 2010; Jurik *et al*, 2015). The ability of GAT1-specific inhibitors to interact within the primary binding site with an altered subsite configuration, demonstrated in this study, gives a clear structural glimpse into the inhibitor specificity of GAT1.

Control of substrate and inhibitor interactions at TM6 linker

The structures of inhibitors complexed to dDAT$_{GAT}$ clearly indicate the importance of the F325L (Leu300 in GAT1$_{WT}$) in regulating the interactions of the substrate and inhibitors in the binding pocket. A comparison of this position among SLC6 members revealed that the biogenic amine transporters have a phenylalanine in this position, whereas the GATs have a substitution to a leucine. The GlyTs, which transport an even smaller neurotransmitter, glycine, have a tryptophan substitution at this position (Trp376^{hGlyT1} and Trp482^{hGlyT2}; Fig 4A). In hGlyT2, it was observed that substitution of the Trp482 to leucine or phenylalanine causes reduced substrate specificity to glycine, thereby allowing a wider range of amino acids to interact with the transporter and elicit currents (Carland *et al*, 2018). The Leu300 in GAT1$_{WT}$ was, therefore, substituted to multiple residues including a phenylalanine, valine, alanine, and tryptophan to analyze the effects on GABA transport activity. The substitution to L300W in GAT1$_{WT}$ yielded a nearly inactive transporter (Fig 4B). A comparison of the dDAT$_{GAT}$ structure with an inhibitor-bound (cmpd1, a derivative of bitopertin), inward-open human GlyT1 (PDB.id 6ZBV) and the AlphaFold2 model of GlyT1 in outward-open state reveals that the Trp376^{hGlyT1} would sterically block the interactions of both inhibitors and substrate within the primary binding site (Fig 4A). In the context of the mutations L300V and L300A, the former substitution is also a branched hydrophobic side chain that would allow interactions of GABA within the binding pocket similar to leucine. Further truncation of this aminoacid side chain to L300A would enhance the volume of the binding pocket allowing the substrate GABA greater flexibility in interactions within the binding pocket leading to weakened interaction affinities likely lowering the uptake activity for ^{3}H-GABA (Fig 4B). We further analyzed the effects of L300F substitution on GAT1 activity and observe that GABA uptake activity is compromised by a twofold increment of K_M to 20.9 μM with a twofold reduction in V_{max} values (Fig 4C and Appendix Table S2). A similar weakening of nipecotic acid inhibition potency was also observed with a 10-fold increment in inhibition constant (134 μM) in nipecotic acid competition of GABA uptake (Fig 4D). Contrary to this behavior, the inhibition constant with bulkier inhibitors like tiagabine, NO711, and SKF89976a displayed a higher inhibition potency indicating an enhanced ability to compete with GABA (Fig 4E–G). This is a likely outcome of L300F in GAT1$_{WT}$ being positioned in a configuration that is similar to the F325L mutant in dDAT$_{GAT}$ and is displaced enough to allow interaction of the inhibitors with subsite C′ in the environment of the GAT1$_{WT}$ binding site. This could be a direct consequence of the F43Y and A117S substitutions having H-bond

interactions with the carbonyl groups of Gly322^{dDAT} and F325L, respectively, in the TM6 linker to facilitate its widening, to allow GAT inhibitor interactions (Fig 2B). This behavior could also be further aided by the reduction of GABA affinity to the L300F that consequently aids in the enhanced ability of the inhibitors to compete for GABA transport.

Allosteric binding site of SKF89976a

The structure of dDAT$_{GAT}$ complexed to SKF89976a displayed an additional density at a second site in the extracellular vestibule of the transporter (Fig 5A and B, and Appendix Fig S3C). The density could clearly fit an additional SKF89976a molecule that forced the displacement of Phe319 to an occluded conformation (Fig 5C and D). The aromatic residues in dDAT$_{GAT}$ Tyr43, Tyr124, and Phe319 form multiple aromatic edge-to-face interactions with the phenyl groups of SKF89976a bound at the primary binding site and the allosteric site in the vestibule (Fig 5D). The N-atom in the nipecotic acid group of SKF89976a interacts with Asp475 directly through a H-bond (3.0 Å). The residue occurs in TM10 and is also conserved in GAT1 (Asp451) and is implicated in the formation of a thin extracellular gate in the vestibule (Ben-Yona & Kanner, 2013). The carboxylate group of SKF89976a indirectly interacts through a water molecule with the E384S residue (Ser359^{GAT1}), which is a substitution we performed in the extracellular vestibule (EL4) of the transporter. A bulk of the residues that surround the SKF89976a in the allosteric site are similar between GAT1$_{WT}$ and dDAT except for an additional residue insertion (Ser456) in the TM10 of GAT1$_{WT}$. The insertion is known to influence efficiency of ion-coupled transport (Dayan *et al*, 2017) and is in proximity to the allosteric site and could also influence the interactions of the inhibitor at the allosteric site, in GAT1$_{WT}$. A comparison of the SKF89976a in the allosteric site with citalopram-bound hSERT (PDB.id 5I73) displays broad similarities in the location of the allosteric site in the vestibule. Interestingly, citalopram interacts with hSERT without disrupting the thin extracellular gate between Arg104^{hSERT} and Glu493^{hSERT} unlike SKF89976a interactions observed in dDAT$_{GAT}$ (Fig 5C). We also observe that the residues in the surrounding environment of citalopram-bound hSERT differ substantially from dDAT$_{GAT}$ that could dictate the differences in specificity toward the two inhibitors (Fig 5C). We decided to investigate whether the allosteric interaction with SKF89976a can be monitored in GAT1$_{WT}$. In order to validate this, we analyzed the alterations in ^{3}H-GABA uptake kinetics in GAT1$_{WT}$ with increasing concentrations of tiagabine, NO711, and SKF89976a using Eadie–Hofstee plots (Figs 5E–G and EV4). Tiagabine and NO711 display competitive inhibition with increasing K_M values but unaltered V_{max} values indicating a clear competitive inhibition propensity with increasing inhibitor concentrations (Figs 5E and F, and EV4). Consequently, increments in SKF89976a displayed both an altered K_M and reduced V_{max} values leading to a behavior that suggests both competitive and noncompetitive components of inhibition of GAT1 by SKF89976a (Fig 5G). This suggests that SKF89976a does interact at an alternate site in GAT1 leading to allosteric inhibition of GABA uptake. Evidence of this behavior was previously noted in multiple experiments involving SKF89976a interactions in GAT1. Interestingly, SKF89976a was observed to be a useful inhibitor to separate stoichiometric transport current and transmitter-mediated Na$^+$ currents in GAT1 and displayed
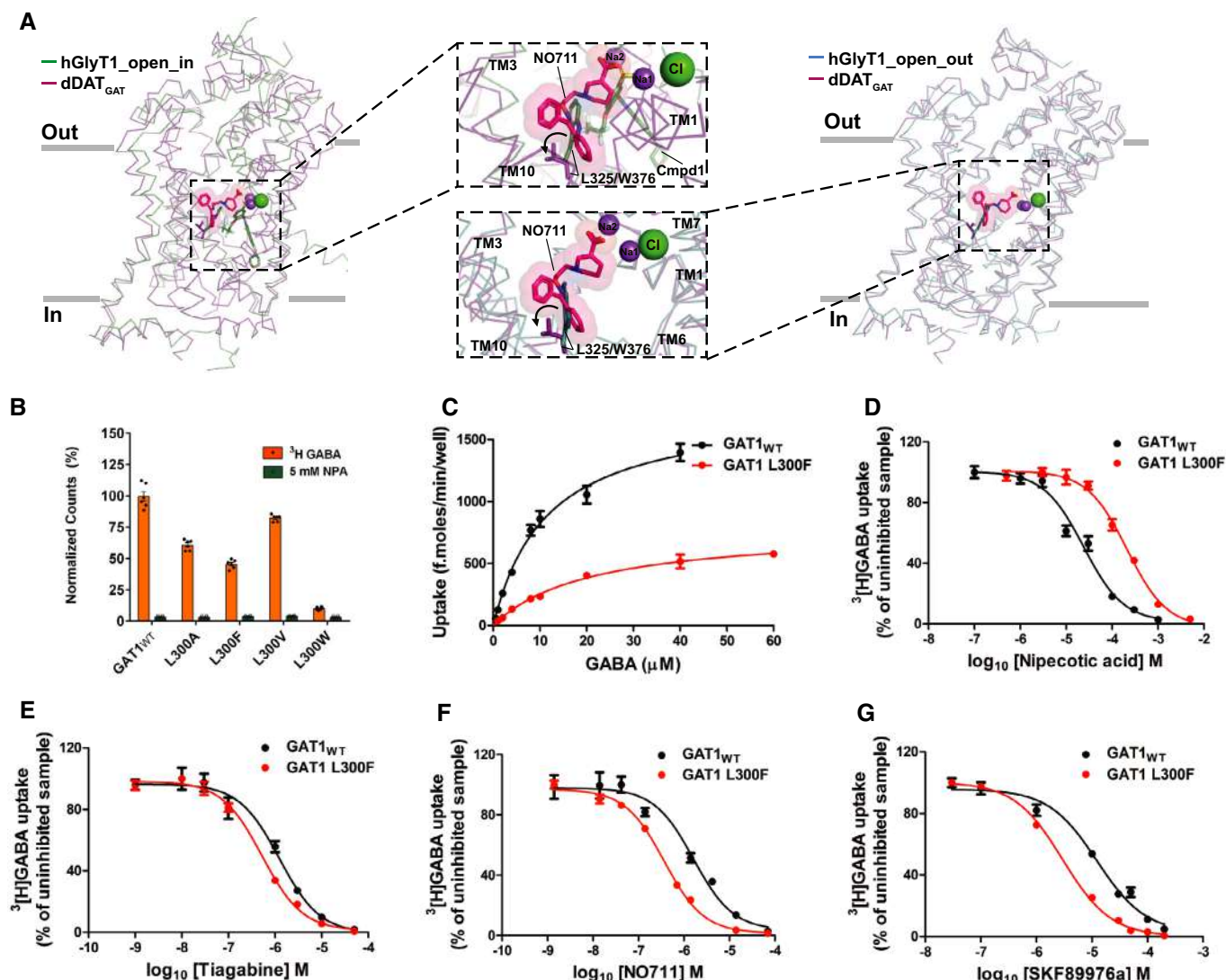
Figure 4. TM6 linker plays a vital role in GABA uptake.

A Side view of structural overlaps between $dDAT_{GAT}$ and hGlyT1 in its inward-open state (PDB id. 6ZBV) with a Cα rmsd of 2.73 Å and hGlyT1 AlphaFold2 model in outward-open state with a Cα rmsd of 1.43 Å. Insets show the presence of W376 in the position of L300 that occludes the substrate binding within the primary binding site and restrict it to smaller substrates like glycine.

B Substitution of L300 to other hydrophobic side chains and the consequences on transport activity. L300W has the maximal effect on the transport activity. The histogram represents mean of a total six measurements ($n = 6$) done as two independent measurements. Individual data points are represented as black dots around the error bar that represents s.e.m.

C–G Changes to Michaelis–Menten kinetics for L300F mutant that displays weakened ^{3}H-GABA uptake activity with $K_M = 20.9$ μM. A near 10-fold loss of nipecotic acid inhibition potency was observed at a value of 134.3 μM. The inhibition potencies of the inhibitors display lowered value suggesting an improved ability to compete for the GABA uptake.

Data information: (C–G) All data plots were performed as two independent experiments each time done in triplicate ($n = 6$). Error bars in the data display s.e.m. Statistical significance of inhibition potencies was measured between the mutant and $GAT1_{WT}$ transporter measured with an unpaired *t*-test display *P* values as follows; nipecotic acid, panel E-0.0001; tiagabine, panel F-0.0017; NO711, panel G-0.018; SKF89976a, panel H-0.0009. $GAT1_{WT}$ transport kinetics and nipecotic acid inhibition potency are redisplayed from Fig 1G–I for comparison. Control data are represented as Appendix Figs S6 and S7.
Source data are available online for this figure.

competitive and noncompetitive modes of inhibiting GAT1 activity (Cammack & Schwartz, 1996; Krause & Schwarz, 2005). It is, therefore, plausible that the SKF89976a binding to the allosteric site in $dDAT_{GAT}$ construct, observed in this study, could provide a rationale for the abilities of this inhibitor to have altered properties in comparison with competitive inhibitors of GAT1 activity.

Selective control of neurotransmitter transport at extracellular loop 4 (EL4)

An analysis of the interactions of SKF89976a bound in the allosteric site reveals that the carboxylate in the nipecotic acid group of SKF89976a faces the EL4 residue at E384S (Ser359^{GAT1}) and
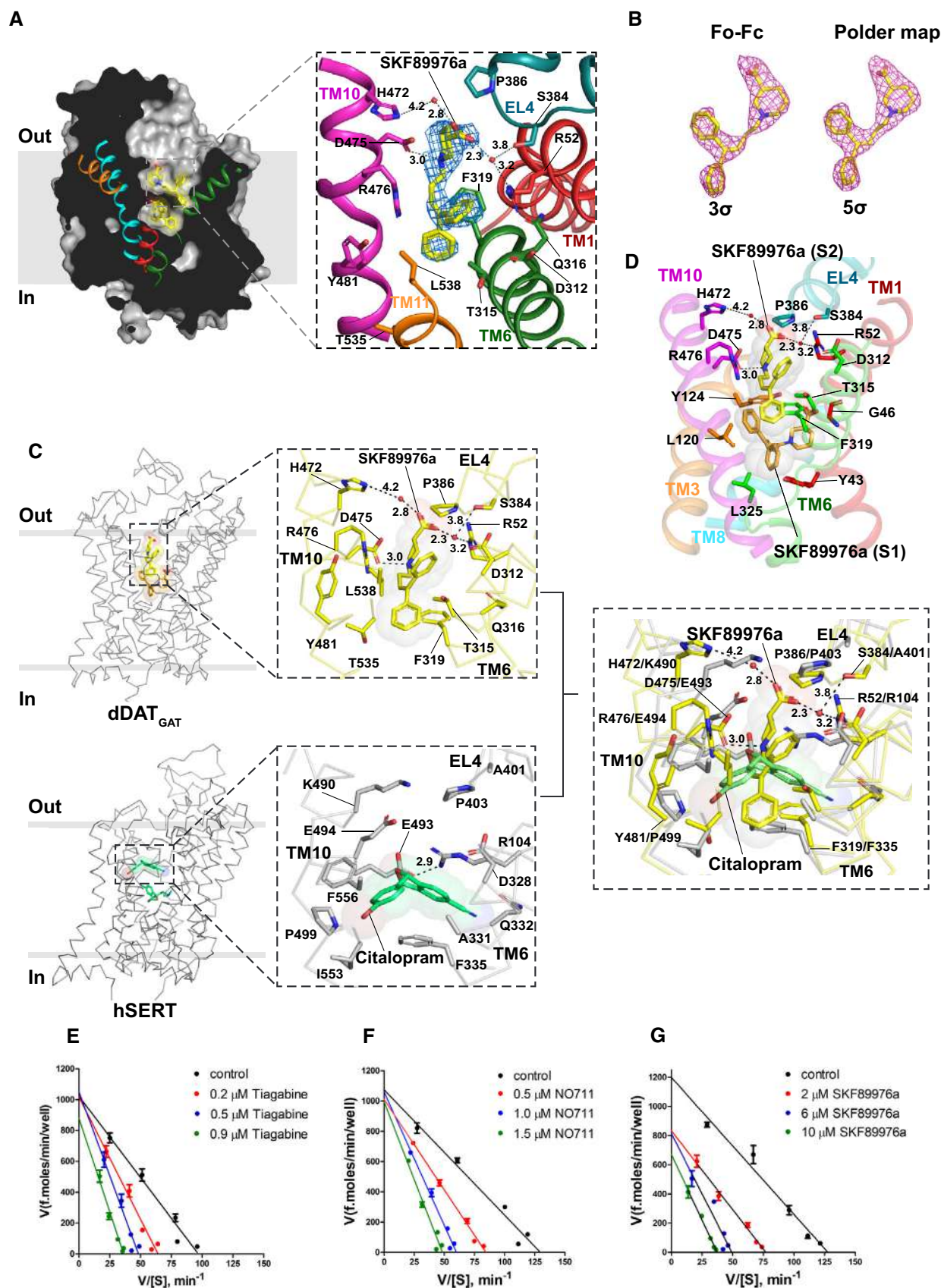
Figure 5.

◄

**Figure 5. Allosteric binding site of SKF89976a.**

A   Longitudinal cross section of SKF89976a-bound dDAT$_{GAT}$ displays proximal interactions of SKF89976a in the allosteric site.
B   *Fo-Fc* and Polder maps of SKF89976a depict the clear presence of the inhibitor in the vestibule.
C   The structures of dDAT$_{GAT}$ in complex with SKF89976a and hSERT in complex with citalopram are shown. Insets show the interactions of residues present in the secondary binding pocket of dDAT$_{GAT}$ and hSERT with SKF89976a and citalopram, respectively. SKF89976a displays a different pose in comparison with the citalopram-bound hSERT but generally coincides with the position of citalopram in the secondary site.
D   Relative positions of the two SKF89976a molecules in the allosteric and primary binding sites interact through a network of aromatic and polar interactions.
E, F   Eadie–Hofstee plots of (E) tiagabine, and (F) NO711 display competitive mode of inhibition of ^{3}H-GABA uptake in GAT1$_{WT}$.
G   Eadie–Hofstee plot of SKF89976a displaying mixed (competitive + noncompetitive) inhibition of ^{3}H-GABA uptake in GAT1$_{WT}$.

Data information: (E–G) Concentrations of the inhibitors were decided based on the K_i values calculated for individual inhibitors. Each data point was plotted using six measurements carried out in two independent measurements in triplicates. Error bars represent s.e.m.
Source data are available online for this figure.

indirectly interacts with the hydroxyl of the serine through a weak water-mediated interaction (3.8 Å; Figs 5D and 6A). The modeled water is also in close proximity (3.2 Å) with guanidine group of Arg52 in TM1b that is conserved in GAT1$_{WT}$ (Arg69; Fig 5A). The EL4 in the recent past has gained prominence as a lid that can control

the association of substrate and inhibitors for selective entry into the extracellular vestibule and interaction of inhibitors in biogenic amine transporters, particularly in the serotonin transporter (Rannversson *et al*, 2015; Esendir *et al*, 2021). Novel allosteric modulators of human dopamine transporter (KM322) are also observed to interact
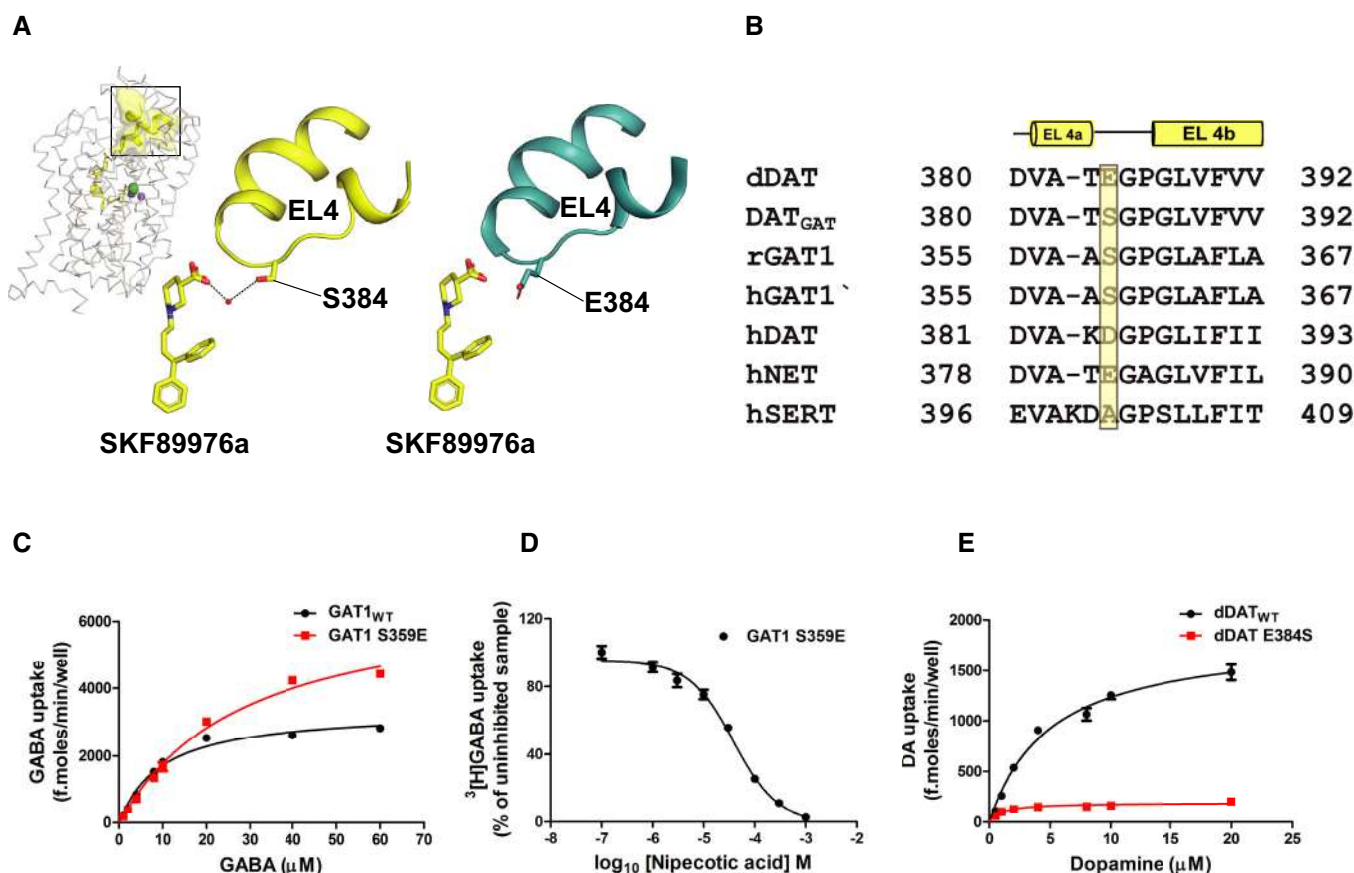
Figure 6. EL4 is involved in neurotransmitter gating.

A   Water-mediated H-bond interactions displayed in SKF89976a interactions with E384S substitution.
B   Alignment shows the presence of acidic side chains in biogenic amine transporters in the EL4.
C   Michaelis–Menten kinetics of GAT1$_{WT}$ and GAT1 S359E displays a weakened K_M value (28.54 ± 2.3 μM). The enhanced V_{max} is a consequence of the enhanced expression of the mutant transporter in the assayed cells monitored by FSEC.
D ^{3}H-GABA uptake inhibition by the substrate analog nipecotic acid for GAT1 S359E displaying a K_i value of 30.1 μM.
E   The equivalent mutation in dDAT$_{WT}$ E384S causes a complete ablation of transport activity despite retaining similar expression levels as dDAT$_{WT}$.

Data information: (C–E) The kinetic plots were plotted as a mean of six measurements carried out in two independent measurements in triplicate. The error bars represent s.e.m.
Source data are available online for this figure.

in the vicinity of EL4 (Asp385[hDAT]), which is the equivalent residue of Glu384[dDAT] (Fig 6B; Aggarwal *et al*, 2019). The proximity of the nipecotic acid moiety of SKF89976a to E384S suggested that the GABA carboxylate and other substrate analogs could interact in a similar fashion (Fig 6A). Superposition of dDAT structure on the dDAT$_{GAT}$ complexed to SKF89976a revealed that the acidic residue at this position, Glu384[dDAT], could alter the interactions with the substrate and affect its entry into the vestibule (Fig 6A and B). This premise was tested through the substitution of S359E in GAT1 and E384S in dDAT$_{WT}$. In GAT1, S359E mutation in EL4a led to a modestly weakened interaction with the substrates indicated by the increased K_M toward GABA, although the V_{max} of the substituted transporter was higher than the GAT1$_{WT}$, which correlated with a proportionate increment in expression level (Figs 6C and EV5A). Interactions of S359E GAT1 with nipecotic acid also displayed a twofold weakening of inhibition potency (30.1 μM) in comparison with the GAT1$_{WT}$ (14.4 μM; Fig 6D and Appendix Table S2C). On the contrary, the dDAT E384S mutation retained similar expression levels but completely compromised the transport activity, highlighting the importance of EL4 in affecting selective entry of neurotransmitters among catecholamine neurotransmitter transporters but less so in the GABA transporter (Figs 6E and EV5B).

Discussion

The structures of the engineered dDAT$_{GAT}$ in complex with tiagabine analogs NO711 and SKF89976a reveal the importance of the residue environment within the primary binding site in dictating inhibitor interactions. We observe the structural consequences of GAT1-like substitutions that shift the trilobed subsite organization for inhibitor interactions to a "bean-shaped" subsite organization (Fig 7A). This is a consequence of minimized access to subsite B and formation of an altered subsite C' due to a widening of the TM6 linker to form a hydrophobic cavity that can interact with the diphenyl aromatic moieties of the two inhibitors of GABA transport, used in this study. Rather interestingly, the disordered region of TM6 reveals yet another modification to facilitate the formation of a new subsite to accommodate GAT1 inhibitors.

The TM6 linker has displayed multiple attributes to regulate the volume and plasticity of the primary binding site in response to substrate and inhibitor interactions observed in earlier studies (Wang *et al*, 2015). In bacterial homologs of SLC6 members like LeuT and MhsT, the residues equivalent to Phe325 (Phe259[LeuT] and Met236[MhsT]) are observed to serve as volumetric sensors that adapt to diverse amino acids binding to the primary binding site (Singh *et al*, 2008; LeVine *et al*, 2019; Focht *et al*, 2021). In the current study, the F325L GAT1-like substitution is in a subtly altered position that avoids clashes with the inhibitor aromatic groups that are ensconced within the TM6 linker in the newly identified subsite C'. This interaction was largely missed by most docking/modeling studies of GAT1 inhibitors with the diaryl moieties generally observed to be docked in the vestibule without completely entering the primary binding site (Skovstrup *et al*, 2010; Jurik *et al*, 2015).

Most antidepressants and psychostimulants that competitively inhibit biogenic amine uptake have interactions with subsite B
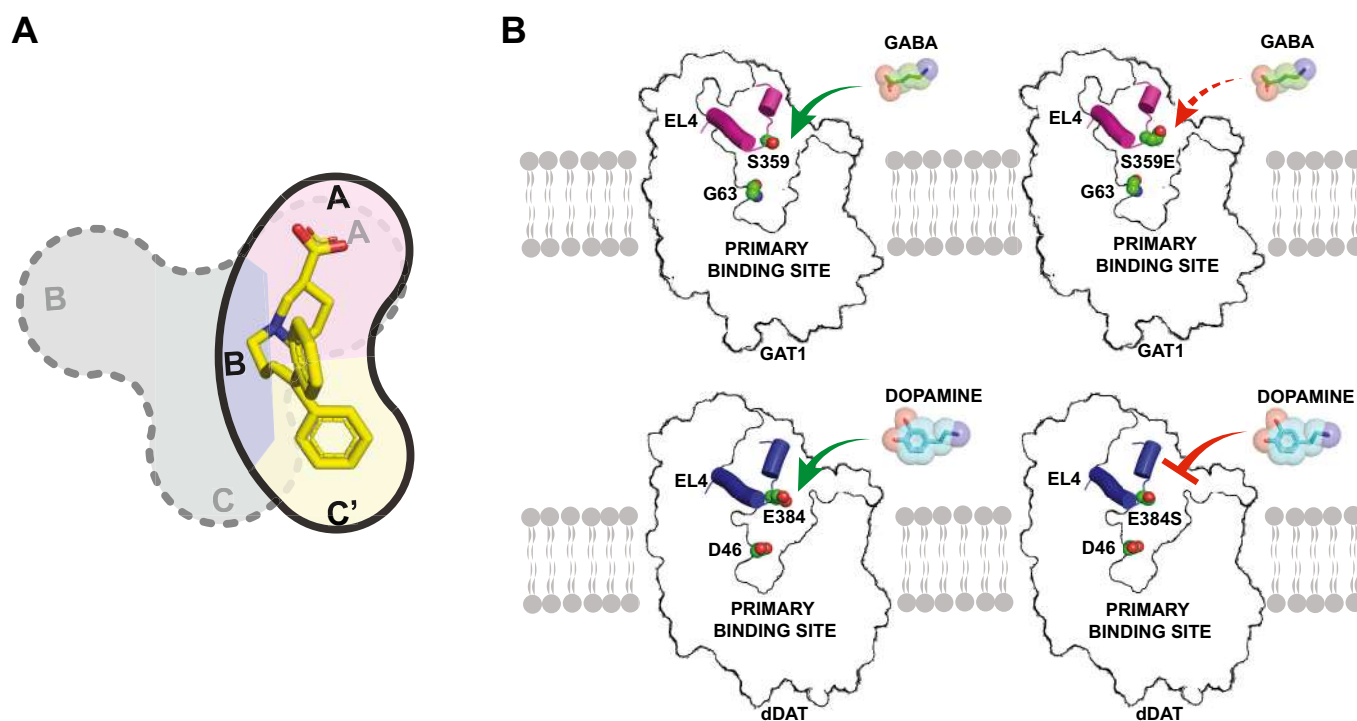

Figure 7. Altered subsite organization and substrate selection at the extracellular vestibule.

A Altered subsite architecture is responsible for the altered inhibitor interactions within the GABA transporter.

B Selective neurotransmitter entry in GABA and biogenic amine transporters is aided by EL4 residues.

wherein aromatic groups interact and enhance the affinity of inhibitors (Wang et al, 2015; Coleman et al, 2016; Pidathala et al, 2021). In the case of GAT1, the polar substitutions in the site create a H-bond network around Thr425 (Thr400^{GAT1}) that disallows any inhibitor interactions in this pocket leading to a major reorganization of the orthosteric binding site.

Despite major alterations within subsites B and C, subsite A remains an important site for substrate recognition in all SLC6 neurotransmitter transporters. In biogenic amine transporters, aspartate residues in TM1b (Asp46^{dDAT} and Asp98^{hSERT}) are involved in recognition of primary and secondary amines in substrates and inhibitors, respectively. The residue is substituted to a glycine in GATs, GlyTs, and bacterial amino acid transporters (Fig EV1). The substitution allows the carboxylate group of the substrate to interact with the Na$^+$ ion at site1 as observed in the NO711 and SKF89976a complexed structures, in this study.

Interestingly, both the inhibitors NO711 and SKF89976a that display high-affinity, sub-micromolar interactions with GAT1 interact with GAT2, GAT3, and BGT1 with significantly weakened affinities (Borden, 1996). The IC50 values for GAT2, GAT3, and BGT1 are 740, 350, and 3,570 μM, respectively, for NO711. SKF89976a displays IC50 values 550, 944, and 7,210 μM against GAT2, GAT3, and BGT1, respectively. Both the inhibitors interact at the primary binding site of GAT1 that has substantial discrepancy in the side chain environment in comparison with GAT2, GAT3, and BGT1 that are closer to each other with similar residue environment in the binding pocket in comparison with GAT1 (Appendix Fig S5). In the region of subsite A, the Tyr60^{GAT1} (Phe43^{dDAT}) forms the base of the primary binding site. This residue is substituted to a glutamate in GAT2, GAT3, and BGT1 (Glu48^{GAT2}, Glu66^{GAT3}, and Glu52^{BGT1}) that substantially alters the charge of the binding pocket and local interactions of –OH group of Tyr60 that forms H-bonds with carbonyl group of TM6 linker residue Gly297^{GAT1} and the hydroxyl side chain of Ser302^{GAT1}. Substitution of Tyr60^{GAT1} to glutamate in GAT1 and the alteration of the Glu48^{GAT2} to a tyrosine in GAT2 led to highly compromised GABA uptake activity (Kanner, 2003; Schlessinger et al, 2012). The aromatic residues at this position, in GAT1 and other biogenic transporters, also form aromatic stacking interactions with the inhibitors that bind in the primary binding site. The substitution to a glutamate in GAT2 and GAT3 disrupts the aforementioned interactions and creates a local negative charge that may hamper carboxylate group containing inhibitors like tiagabine, NO711, and SKF89976a (Latka et al, 2020b). Further modifications include the presence of a glycine (Gly297^{GAT1}) substituted to alanine in the TM6a of GAT2 and GAT3 (Ala291^{GAT2}, Ala311^{GAT3}, and Ala296^{BGT1}) that constrict the space for nipecotic acid binding in comparison with GAT1. We also observe multiple substitutions of GAT1 residues in the binding pocket to cysteine that include Gly299^{GAT1} (substituted to Cys293^{GAT2}, Cys313^{GAT3}, and Cys298^{BGT1}); Ser302^{GAT1} (equivalent to Cys296^{GAT2}, Cys316^{GAT3}, and Cys301^{BGT1}); and Thr400^{GAT1} (equivalent to Cys394^{GAT2}, Cys414^{GAT3}, and Cys399^{BGT1}). Although the models do not indicate the presence of a disulfide bond among the cysteine residues in the binding sites of GAT2, GAT3, and BGT1, future structural studies on these isoforms may reveal disulfide cross-links within the binding pocket. These substitutions significantly alter the polar and hydrophobic interactions of the inhibitor binding site and disrupt the H-bond networks formed by the residues in the direct vicinity of the inhibitor, likely leading to weakened interactions of GAT1-specific inhibitors.

The complex of dDAT$_{GAT}$ with SKF89976a provided a serendipitous observation of the inhibitor bound in the allosteric site in addition to the orthosteric site. Unlike the primary binding site in dDAT$_{GAT}$ that carries 10 GAT1-like substitutions, the extracellular vestibule was left largely unaltered and a single substitution was done in EL4 (E384S). Allosteric sites modulating neurotransmitter transport have gained prominence in the recent past with the identification of citalopram, vilazodone binding in hSERT at the allosteric site in the vestibule (Coleman et al, 2016; Plenge et al, 2021). Diverse interactions of noncompetitive inhibitors were also mapped in GlyTs with cmpd1 interacting with an inward-open state and bioactive lipids proposed to interact with GlyT2 (Mostyn et al, 2019; Shahsavar et al, 2021). Although allosteric inhibitors of GABA uptake have also been characterized using mass spectroscopy-based tools, their exact site of interaction is unknown due to the absence of a structure for any GAT isoform (Hauke et al, 2018). The SKF89976a bound in the allosteric site in the extracellular vestibule of dDAT$_{GAT}$ can, therefore, aid in understanding allosteric inhibitors of GAT1. This is particularly important as SKF89976a was previously known to interact with GAT1 in both a competitive and noncompetitive manner and differentiate between GABA transport current and GABA evoked inward Na$^+$ currents observed in GATs (Cammack & Schwartz, 1996; Eckstein-Ludwig et al, 1999; Krause & Schwarz, 2005).

The interactions of the nipecotic acid moiety of SKF89976a, in the allosteric site with the E384S substitution, were investigated, and the results indicate that residues in EL4 region could be an additional site of control of neurotransmitter entry in dDAT but less so in GAT1. The negative charge of Glu384^{dDAT} in EL4 could also aid in attracting the positively charged monoamines to enter the vestibule. In DAT and SERT, the rate-limiting step of substrate/inhibitor selectivity is observed to be the association rate (Hasenhuetl et al, 2015). EL4, due to its unique position to plug the extracellular vestibule can affect association rates and thereby substrate/inhibitor interactions within the transporter. Evidence of this is visible in EL4 of hSERT where substitutions (L406E) are observed to weaken substrate transport and allow competitive inhibitors to interact with increased potency through stabilizing the outward-open state (Rannversson et al, 2015). However, our observations with equivalent EL4 substitutions in dDAT and GAT1 indicate that the two transporters behave rather distinctly in response to changes in EL4 with GAT1 showing a modest effect on substrate interactions and transport activity, whereas the dDAT displaying complete loss of dopamine uptake (Fig 7B). Insights into these distinct substrate translocation effects within the extracellular vestibule and the details of allosteric inhibitor interactions could be provided through future structural studies of GAT isoforms.

While an engineered construct of dDAT$_{GAT}$ may not be a perfect substitute to study the diverse aspects of GAT1 structure and function, we could successfully translocate and mimic a GAT1 binding site into a catecholamine transporter, dDAT, to unravel some unknown facets of GAT pharmacology. The structures of GAT inhibitors complexed to dDAT$_{GAT}$ can serve as templates for improved designs of allosteric and orthosteric modulators of GAT activity. This is particularly significant in the context of GABA transport inhibition being a major strategy for treatment of epileptic conditions like partial seizures.

Materials and Methods

Constructs used in the study

The *Drosophila melanogaster* dopamine transporter (dDAT) construct used for dDAT$_{GAT}$ engineering (*dDAT TS2*) contains a deletion of 20 amino acids in the N terminus (Δ1–20), a deletion in the extracellular loop 2 (EL2) from 164 to 191 amino acids (Δ164–191) and also contains two thermostabilizing mutations, V74A and L415A. The dDAT$_{GAT}$ construct used for crystallization studies consists of 11 substitutions that include F43Y, D46G, A117S, V120L, D121N, F325L, V327S, E384S, S422Q, G425T, and S426V. In addition to these 11 mutations, the construct has deletions Δ1–20 and Δ162–202 and thermostabilizing mutations V74A, V275A, V311A, L415A, and G538L. Residues 602–607 were replaced with a thrombin site (LVPRGS) toward the C terminus. All the dDAT mutants generated for dDAT$_{GAT}$ engineering are mentioned in Appendix Table S1.

The dDAT$_{mfc}$ construct contains five thermostabilizing mutations, V74A, V275A, V311A, L415A, and G538L and deletions Δ1–20 and Δ162–202. A thrombin site (LVPRGS) was inserted by replacing residues from 602 to 607.

The *Rattus norvegicus* GABA transporter 1 (*GAT1$_{WT}$*) gene used for the biochemical studies was subcloned into pEG-BacMam vector between EcoR1 and Not1 restriction sites from pBluescript II vector.

Purification of dDAT$_{GAT}$

The dDAT$_{GAT}$ construct was expressed as a C-terminal GFP fusion protein in HEK293 GnTI$^-$ cell lines using baculovirus-mediated expression system (Goehring *et al*, 2014). Membranes were solubilized in 20 mM dodecyl β-D-maltoside (DDM; Anatrace), 2 mM cholesteryl hemisuccinate (CHS; Anatrace), 50 mM Tris-Cl pH 8.0, 150 mM NaCl, and 0.1 mM PMSF by incubating for 2 h. The solubilized material was separated by ultracentrifugation at 100,000 × *g* for 90 min. The supernatant was affinity-purified using Talon resin (pre-equilibrated with 1× TBS) in 20 mM Tris-Cl pH 8.0, 300 mM NaCl, 100 mM imidazole, 1% glycerol buffer containing 1 mM DDM, and 0.2 mM CHS. The affinity-purified dDAT$_{GAT}$ protein was treated with thrombin (Haematologic Technologies Inc) for 36 h at 4°C in order to cleave the GFP-8x-His tag at the C-terminal. The cleaved protein was concentrated to 4 mg/ml and injected into a Superdex-200 10/300 increase column (GE Life Sciences), which was pre-equilibrated with size-exclusion chromatography (SEC) buffer containing 20 mM Tris-Cl pH 8.0, 300 mM NaCl, 5% Glycerol, 4 mM decyl-β-D-maltoside (DM), 0.3 mM CHS, and 0.01% (w/v) 1-pamitoyl-2-oleoyl-*sn*-glycero-3-phospho ethanolamine (POPE; Avanti Polar Lipids).

Expression and purification of Fab

Heterologous expression of the Fab 9D5 was carried out using baculovirus-mediated insect cell expression system (Pidathala *et al*, 2021; Appendix Fig S2D). Fab heavy and light chain genes were synthesized (Genscript) and cloned into pFastBac Dual vector. The heavy chain is under the polyhedrin promoter, and the light chain is under the P10 promoter along with N-terminal GP64 signal sequence on each chain. Sf9 cells in suspension media at a density

of 2.5 × 10^6 cells/ml were infected using high titer recombinant baculovirus, and the supernatant containing Fab was dialyzed against 25 mM Tris-Cl (pH 8.0) and 50 mM NaCl. The Fab (9D5) was affinity-purified from the dialysate using metal ion affinity chromatography in 25 mM Tris-Cl (pH 8.0), 50 mM NaCl, and 250 mM imidazole. The affinity-purified Fab was further purified using size-exclusion chromatography by injecting into a superdex 75 10/300 GL column (GE Life Sciences) in 25 mM Tris-Cl (pH 8.0) and 50 mM NaCl.

Crystallization and structure determination

Purified dDAT$_{GAT}$ was incubated with varying concentrations of GAT1 inhibitors, NO711 and SKF89976a for 3 h at 4°C on prior to the addition of Fab 9D5 in a molar ratio of 1:1.2. The dDAT$_{GAT}$-9D5 complex was incubated on ice for 30 min and concentrated to a final concentration of 3.0–3.5 mg/ml using a 100 kDa cutoff centrifugal concentrator (Amicon Ultra). The concentrated protein complex was ultra-centrifuged at 100,000 × *g* for 60 min and subjected to crystallization using hanging drop vapor diffusion method at 4°C. The dDAT$_{GAT}$ substrate-free form and dDAT$_{GAT}$-NO-711-bound crystals were obtained in 0.1 M MOPS pH 6.5–7.0 and 32–34% PEG 600, whereas dDAT$_{GAT}$-SKF89976a-bound crystals were obtained in 0.1 M Tris-Bicine pH 8.0–8.2 and 32–34% PEG 600. Cocrystallization of inhibitors with dDAT$_{GAT}$ was performed in the presence of 0.5 mM of both inhibitors. X-ray diffraction data sets were collected at 24IDC at APS and XRD2, Elettra and crystals diffracted in a resolution range of 2.8–3.2 Å (Appendix Table S3). X-ray data were processed using XDS, and scaling and merging were performed using AIMLESS in the CCP4 software suite (Kabsch, 2010; Evans & Murshudov, 2013). The dDAT$_{GAT}$ structures were solved using molecular replacement by PHASER with the dDAT and 9D5 coordinates from PDB id 4XNU (McCoy *et al*, 2007). After fitting the ligands in the omit densities, multiple rounds of refinement were carried out using Phenix.refine and COOT in the PHENIX crystallographic software suite, respectively (Adams *et al*, 2010). Ligand fitting was done in COOT followed by real-space refinement after fitting the inhibitor generated using SMILES. The real-space correlation coefficient for the inhibitors in the dDAT$_{GAT}$ structures is above 0.85.

GABA uptake assay

The uptake assays were performed using HEK 293 GnTI$^-$ cells expressing respective constructs. Cells were resuspended in 25 mM HEPES-Tris pH 7.1, 130 mM NaCl, 1 mM MgSO$_4$, 5 mM KCl, 1 mM CaCl$_2$, and 5 mM D-Glucose containing uptake assay buffer. Control samples were pre-incubated with 10 μM of tiagabine for 30 min before addition of radiolabel. One micrometre of GABA in a 1:200 molar ratio of [^{3}H]-GABA: [^{1}H]-GABA (Perkin Elmer) was added and incubated for 30 min at room temperature. The reaction was arrested by the addition of ice-cold assay buffer, and the cells were washed twice with the same buffer before solubilizing in 20 mM DDM. The solubilized sample was separated using centrifugation at 14,500 × *g* for 30 min, and the supernatant was added to 0.5 ml of scintillation fluid (Ultima Gold, Perkin Elmer). The radioactive counts were measured by liquid scintillation counting using MicroBeta scintillation counter (Perkin Elmer).

GABA uptake and inhibition assay in 96-well plate format

For the determination of K_M, K_i, and V_{max} values, the GABA uptake assays were carried out in 96-well plates (Aggarwal & Mortensen, 2017). HEK 293 GnTI$^-$ cells were infected with the baculovirus of respective mutant, and cells were plated at a cell density of 50,000 cells per well 36-h post-infection. Uninfected cells were used as the control. The media were aspirated after 4 h, and the cells were washed with assay buffer containing 25 mM HEPES-Tris pH 7.1, 130 mM NaCl, 1 mM MgSO$_4$, 5 mM KCl, 1 mM CaCl$_2$, and 5 mM D-Glucose. The cells were incubated with varying concentrations of GABA (0.5, 1, 2, 4, 8, 10, 20, and 40 μM) in 1:500 molar ratios of [^{3}H-GABA] and [^{1}H GABA] and incubated for 15 min at room temperature. GABA uptake was arrested with 200 μl of ice-cold assay buffer and washed twice with the same buffer before solubilization. Fifty microlitre of scintillation fluid was added to the solubilized material, and the radioactivity was estimated by scintillation counting using MicroBeta liquid scintillation counter. The background-subtracted initial uptake rates were plotted against the above-mentioned concentrations of GABA to determine the K_M and V_{max} values. The data were plotted and analyzed using GraphPad Prism v.5.0.1.

For the estimation of K_i value, we carried out GABA uptake assays in 96-well plate format as described above. The cells were incubated in the uptake assay buffer containing varying concentrations of inhibitors for 30 min. This was followed by the addition of 8 μM GABA in 1:500 molar ratios of [^{3}H-GABA] and [^{1}H GABA] and incubated for 15 min at room temperature. The reaction was arrested with the ice-cold assay buffer and washed with the same buffer before solubilization. Fifty microlitre of scintillation fluid was added to the solubilized material, and the radioactive counts were estimated on MicroBeta liquid scintillation counter. The background-subtracted, dose–response plots were analyzed and plotted using GraphPad Prism v.5.0.1, and K_i values were determined from Cheng-Prusoff's equation using the IC$_{50}$ values obtained from the experiments.

Dopamine uptake assay

The assay was carried out with the wild-type and mutant dopamine transporter for the determination of K_M and V_{max} values using the uptake assay (96-well plate format) described in the previous section. Dopamine uptake was initiated by the addition of varying concentrations of DA (0.5, 1, 2, 4, 8, 10, and 20 μM) in 1:200 molar ratios of [^{3}H]-DA: [^{1}H]-DA at room temperature. The uptake was arrested after 5 min with the ice-cold uptake buffer containing 200 μl of 25 mM HEPES-Tris pH 7.1, 130 mM NaCl, 1 mM MgSO$_4$, 5 mM KCl, 1 mM CaCl$_2$, 5 mM D-Glucose, 1 mM ascorbic acid, and 30 μM pargyline, and the cells were washed twice with the same buffer before solubilization. Fifty microlitre of scintillation fluid was added to the solubilized material, and the radioactivity was estimated on MicroBeta scintillation counter. The background-subtracted initial uptake rates were plotted against the respective DA concentration, and values of K_M were determined.

Binding assay

Binding assay for the dDAT$_{GAT}$ construct was carried out using microscale thermophoresis (MST; Nanotemper; Clémençon

et al, 2018). 100 nM of SEC purified dDAT$_{GAT}$ was labeled with 100 nM red Tris-NTA dye. The labeled protein was incubated with 16 twofold serial dilution of the ligand keeping the protein concentration constant at 10 nM. Monolith™ NT.115 MST premium-coated capillaries were used in all the experiments. The starting concentrations of ligands were 2 mM and dissolved in the same buffer as that of the protein (50 mM HEPES pH 8.0, 300 mM NaCl, 5% Glycerol, 4 mM DM, 0.3 mM CHS, and 0.01% (w/v) 1-pamitoyl-2-oleoyl-sn-glycero-3-phospho ethanolamine (POPE)). The thermophoresis binding data were analyzed and plotted using Graphpad Prism. The dDAT$_{mfc}$ construct was used as the control for MST binding assays.

Homology modeling

The homology models of GAT isoforms GAT2, GAT3, and BGT1 were built using the dDAT$_{GAT}$ structures as templates in the swiss-model online server (https://swissmodel.expasy.org/). The resulting models had very close overlap on the template structure with all greater than 98% of residues in the favored regions of the Ramachandran plot. The human GlyT1 outward-open model used for structural comparison was obtained from the AlphaFold2 database (https://alphafold.ebi.ac.uk/; Varadi et al, 2022).

Data availability

The coordinates for the structures have been deposited in the Protein Data Bank with the following accession codes 7WGD, 7WGT, and 7WLW (Appendix Table S3). The raw data and gel images for all biochemical experiments have been deposited alongside the manuscript as supplementary information and a source data file. Diffraction data would be made available upon request.

Data statistics

All the radiolabel biochemical assays were performed as two independent measurements each done in triplicate. All six measurements of individual data points were used to calculate the transport and inhibition parameters in the study using GraphPad Prism v.5.0.1. The error bars in all cases represent s.e.m, and unpaired two-tailed t-tests were performed to calculate significance values.

Expanded View for this article is available online.

Author contributions

Disclosure and competing interests statement

References

Adams PD, Afonine PV, Bunkoczi G, Chen VB, Davis IW, Echols N, Headd JJ, Hung LW, Kapral GJ, Grosse-Kunstleve RW *et al* (2010) PHENIX: a comprehensive python-based system for macromolecular structure solution. *Acta Crystallogr D Biol Crystallogr* 66: 213 – 221

Aggarwal S, Liu X, Rice C, Menell P, Clark PJ, Paparoidamis N, Xiao YC, Salvino JM, Fontana ACK, Espana RA *et al* (2019) Identification of a novel allosteric modulator of the human dopamine transporter. *ACS Chem Neurosci* 10: 3718 – 3730

Aggarwal S, Mortensen OV (2017) In vitro assays for the functional characterization of the dopamine transporter (DAT). *Curr Protoc Pharmacol* 79: 12.17.1 – 12.17.21

Ali FE, Bondinell WE, Dandridge PA, Frazee JS, Garvey E, Girard GR, Kaiser C, Ku TW, Lafferty JJ, Moonsammy GI *et al* (1985) Orally active and potent inhibitors of gamma-aminobutyric acid uptake. *J Med Chem* 28: 653 – 660

Ben-Ari Y (2002) Excitatory actions of gaba during development: the nature of the nurture. *Nat Rev Neurosci* 3: 728 – 739

Ben-Yona A, Kanner BI (2013) Functional defects in the external and internal thin gates of the gamma-aminobutyric acid (GABA) transporter GAT-1 can compensate each other. *J Biol Chem* 288: 4549 – 4556

Bentzen BH, Grunnet M (2011) Central and peripheral GABA(a) receptor regulation of the heart rate depends on the conscious state of the animal. *Adv Pharmacol Sci* 2011: 578273

Bettler B, Kaupmann K, Mosbacher J, Gassmann M (2004) Molecular structure and physiological functions of GABA(B) receptors. *Physiol Rev* 84: 835 – 867

Bhat R, Axtell R, Mitra A, Miranda M, Lock C, Tsien RW, Steinman L (2010) Inhibitory role for GABA in autoimmune inflammation. *Proc Natl Acad Sci USA* 107: 2580 – 2585

Bismuth Y, Kavanaugh MP, Kanner BI (1997) Tyrosine 140 of the gamma-aminobutyric acid transporter GAT-1 plays a critical role in neurotransmitter recognition. *J Biol Chem* 272: 16096 – 16102

Borden LA (1996) GABA transporter heterogeneity: pharmacology and cellular localization. *Neurochem Int* 29: 335 – 356

Borden LA, Murali Dhar TG, Smith KE, Weinshank RL, Branchek TA, Gluchowski C (1994) Tiagabine, SK&F 89976-a, CI-966, and NNC-711 are selective for the cloned GABA transporter GAT-1. *Eur J Pharmacol* 269: 219 – 224

Cammack JN, Schwartz EA (1996) Channel behavior in a gamma-aminobutyrate transporter. *Proc Natl Acad Sci USA* 93: 723 – 727

Carland JE, Thomas M, Mostyn SN, Subramanian N, O'Mara ML, Ryan RM, Vandenberg RJ (2018) Molecular determinants for substrate interactions with the glycine transporter GlyT2. *ACS Chem Neurosci* 9: 603 – 614

Clausen RP, Madsen K, Larsson OM, Frolund B, Krogsgaard-Larsen P, Schousboe A (2006) Structure-activity relationship and pharmacology of gamma-aminobutyric acid (GABA) transport inhibitors. *Adv Pharmacol* 54: 265 – 284

Clémençon B, Lüscher BP, Hediger MA (2018) Establishment of a novel microscale thermophoresis ligand-binding assay for characterization of SLC solute carriers using oligopeptide transporter PepT1 (SLC15 family) as a model system. *J Pharmacol Toxicol Methods* 92: 67 – 76

Coleman JA, Green EM, Gouaux E (2016) X-ray structures and mechanism of the human serotonin transporter. *Nature* 532: 334 – 339

Dalby NO (2003) Inhibition of gamma-aminobutyric acid uptake: anatomy, physiology and effects against epileptic seizures. *Eur J Pharmacol* 479: 127 – 137

Dayan O, Nagarajan A, Shah R, Ben-Yona A, Forrest LR, Kanner BI (2017) An extra amino acid residue in transmembrane domain 10 of the gamma-aminobutyric acid (GABA) transporter GAT-1 is required for efficient ion-coupled transport. *J Biol Chem* 292: 5418 – 5428

Eckstein-Ludwig U, Fei J, Schwarz W (1999) Inhibition of uptake, steady-state currents, and transient charge movements generated by the neuronal GABA transporter by various anticonvulsant drugs. *Br J Pharmacol* 128: 92 – 102

Esendir E, Burtscher V, Coleman JA, Zhu R, Gouaux E, Freissmuth M, Sandtner W (2021) Extracellular loops of the serotonin transporter act as a selectivity filter for drug binding. *J Biol Chem* 297: 100863

Evans PR, Murshudov GN (2013) How good are my data and what is the resolution? *Acta Crystallogr D Biol Crystallogr* 69: 1204 – 1214

Florey E, Mc LH (1959) The effects of factor I and of gamma-aminobutyric acid on smooth muscle preparations. *J Physiol* 145: 66 – 76

Focht D, Neumann C, Lyons J, Eguskiza Bilbao A, Blunck R, Malinauskaite L, Schwarz IO, Javitch JA, Quick M, Nissen P (2021) A non-helical region in transmembrane helix 6 of hydrophobic amino acid transporter MhsT mediates substrate recognition. *EMBO J* 40: e105164

Goehring A, Lee CH, Wang KH, Michel JC, Claxton DP, Baconguis I, Althoff T, Fischer S, Garcia KC, Gouaux E (2014) Screening and large-scale expression of membrane proteins in mammalian cells for structural studies. *Nat Protoc* 9: 2574 – 2585

Guastella J, Nelson N, Nelson H, Czyzyk L, Keynan S, Miedel MC, Davidson N, Lester HA, Kanner BI (1990) Cloning and expression of a rat brain GABA transporter. *Science* 249: 1303–1306

Hasenhuetl PS, Schicker K, Koenig X, Li Y, Sarker S, Stockner T, Sucic S, Sitte HH, Freissmuth M, Sandtner W (2015) Ligand selectivity among the dopamine and serotonin transporters specified by the forward binding reaction. *Mol Pharmacol* 88: 12–18

Hauke TJ, Wein T, Hofner G, Wanner KT (2018) Novel allosteric ligands of gamma-aminobutyric acid transporter 1 (GAT1) by MS based screening of Pseudostatic Hydrazone libraries. *J Med Chem* 61: 10310–10332

Hilgemann DW, Lu CC (1999) GAT1 (GABA:Na$^+$:Cl$^-$) cotransport function. Database reconstruction with an alternating access model. *J Gen Physiol* 114: 459–475

Hyland NP, Cryan JF (2010) A gut feeling about GABA: focus on GABA(B) receptors. *Front Pharmacol* 1: 124

Iversen LL, Neal MJ (1968) The uptake of [3H]GABA by slices of rat cerebral cortex. *J Neurochem* 15: 1141–1149

Jacob TC, Moss SJ, Jurd R (2008) GABA(a) receptor trafficking and its role in the dynamic modulation of neuronal inhibition. *Nat Rev Neurosci* 9: 331–343

Joseph D, Pidathala S, Mallela AK, Penmatsa A (2019) Structure and gating dynamics of Na(+)/Cl(−) coupled neurotransmitter transporters. *Front Mol Biosci* 6: 80

Jurik A, Zdrazil B, Holy M, Stockner T, Sitte HH, Ecker GF (2015) A binding mode hypothesis of tiagabine confirms liothyronine effect on gamma-aminobutyric acid transporter 1 (GAT1). *J Med Chem* 58: 2149–2158

Kabsch W (2010) XDS. *Acta Crystallogr D Biol Crystallogr* 66: 125–132

Kanner BI (2003) Transmembrane domain I of the gamma-aminobutyric acid transporter GAT-1 plays a crucial role in the transition between cation leak and transport modes. *J Biol Chem* 278: 3705–3712

Kavanaugh MP, Arriza JL, North RA, Amara SG (1992) Electrogenic uptake of gamma-aminobutyric acid by a cloned transporter expressed in xenopus oocytes. *J Biol Chem* 267: 22007–22009

Khazipov R (2016) GABAergic synchronization in epilepsy. *Cold Spring Harb Perspect Med* 6: a022764

Krause S, Schwarz W (2005) Identification and selective inhibition of the channel mode of the neuronal GABA transporter 1. *Mol Pharmacol* 68: 1728–1735

Kristensen AS, Andersen J, Jorgensen TN, Sorensen L, Eriksen J, Loland CJ, Stromgaard K, Gether U (2011) SLC6 neurotransmitter transporters: structure, function, and regulation. *Pharmacol Rev* 63: 585–640

Krnjević K, Schwartz S (1967) The action of γ-Aminobutyric acid on cortical neurones. *Exp Brain Res* 3: 320–336

Krogsgaard-Larsen P (1980) Inhibitors of the GABA uptake systems. *Mol Cell Biochem* 31: 105–121

Latka K, Jonczyk J, Bajda M (2020a) Gamma-aminobutyric acid transporters as relevant biological target: their function, structure, inhibitors and role in the therapy of different diseases. *Int J Biol Macromol* 158: 750–772

Latka K, Jonczyk J, Bajda M (2020b) Structure modeling of gamma-aminobutyric acid transporters − molecular basics of ligand selectivity. *Int J Biol Macromol* 158: 1380–1389

LeVine MV, Terry DS, Khelashvili G, Siegel ZS, Quick M, Javitch JA, Blanchard SC, Weinstein H (2019) The allosteric mechanism of substrate-specific transport in SLC6 is mediated by a volumetric sensor. *Proc Natl Acad Sci USA* 116: 15947–15956

Lu CC, Hilgemann DW (1999) GAT1 (GABA:Na$^+$:Cl$^-$) cotransport function. Kinetic studies in giant xenopus oocyte membrane patches. *J Gen Physiol* 114: 445–457

McCoy AJ, Grosse-Kunstleve RW, Adams PD, Winn MD, Storoni LC, Read RJ (2007) Phaser crystallographic software. *J Appl Cryst* 40: 658–674

Mostyn SN, Wilson KA, Schumann-Gillett A, Frangos ZJ, Shimmon S, Rawling T, Ryan RM, O'Mara ML, Vandenberg RJ (2019) Identification of an allosteric binding site on the human glycine transporter, GlyT2, for bioactive lipid analgesics. *eLife* 8: e47150

Owens DF, Kriegstein AR (2002) Is there more to GABA than synaptic inhibition? *Nat Rev Neurosci* 3: 715–727

Penmatsa A, Wang KH, Gouaux E (2013) X-ray structure of dopamine transporter elucidates antidepressant mechanism. *Nature* 503: 85–90

Pidathala S, Mallela AK, Joseph D, Penmatsa A (2021) Structural basis of norepinephrine recognition and transport inhibition in neurotransmitter transporters. *Nat Commun* 12: 2199

Plenge P, Yang D, Salomon K, Laursen L, Kalenderoglou IE, Newman AH, Gouaux E, Coleman JA, Loland CJ (2021) The antidepressant drug vilazodone is an allosteric inhibitor of the serotonin transporter. *Nat Commun* 12: 5063

Rannversson H, Wilson P, Kristensen KB, Sinning S, Kristensen AS, Stromgaard K, Andersen J (2015) Importance of the extracellular loop 4 in the human serotonin transporter for inhibitor binding and substrate translocation. *J Biol Chem* 290: 14582–14594

Schlessinger A, Wittwer MB, Dahlin A, Khuri N, Bonomi M, Fan H, Giacomini KM, Sali A (2012) High selectivity of the γ-aminobutyric acid transporter 2 (GAT-2, SLC6A13) revealed by structure-based approach. *J Biol Chem* 287: 37745–37756

Scimemi A (2014) Plasticity of GABA transporters: an unconventional route to shape inhibitory synaptic transmission. *Front Cell Neurosci* 8: 128

Shahsavar A, Stohler P, Bourenkov G, Zimmermann I, Siegrist M, Guba W, Pinard E, Sinning S, Seeger MA, Schneider TR et al (2021) Structural insights into the inhibition of glycine reuptake. *Nature* 591: 677–681

Singh SK, Piscitelli CL, Yamashita A, Gouaux E (2008) A competitive inhibitor traps LeuT in an open-to-out conformation. *Science* 322: 1655–1661

Skovstrup S, Taboureau O, Brauner-Osborne H, Jorgensen FS (2010) Homology modelling of the GABA transporter and analysis of tiagabine binding. *ChemMedChem* 5: 986–1000

Soudijn W, van Wijngaarden I (2000) The GABA transporter and its inhibitors. *Curr Med Chem* 7: 1063–1079

Sperk G, Furtinger S, Schwarzer C, Pirker S (2004) GABA and its receptors in epilepsy. *Adv Exp Med Biol* 548: 92–103

Suzdak PD, Jansen JA (1995) A review of the preclinical pharmacology of tiagabine: a potent and selective anticonvulsant GABA uptake inhibitor. *Epilepsia* 36: 612–626

Treiman DM (2001) GABAergic mechanisms in epilepsy. *Epilepsia* 42 Suppl 3: 8–12

Varadi M, Anyango S, Deshpande M, Nair S, Natassia C, Yordanova G, Yuan D, Stroe O, Wood G, Laydon A et al (2022) AlphaFold protein structure database: massively expanding the structural coverage of protein-sequence space with high-accuracy models. *Nucleic Acids Res* 50: D439–D444

Wang H, Goehring A, Wang KH, Penmatsa A, Ressler R, Gouaux E (2013) Structural basis for action by diverse antidepressants on biogenic amine transporters. *Nature* 503: 141–145

Wang KH, Penmatsa A, Gouaux E (2015) Neurotransmitter and psychostimulant recognition by the dopamine transporter. *Nature* 521: 322−327

Yamashita A, Singh SK, Kawate T, Jin Y, Gouaux E (2005) Crystal structure of a bacterial homologue of Na^+/Cl^--dependent neurotransmitter transporters. *Nature* 437: 215−223

Zafar S, Jabeen I (2018) Structure, function, and modulation of gamma-aminobutyric acid transporter 1 (GAT1) in neurological disorders: a pharmacoinformatic prospective. *Front Chem* 6: 397

Zhou Y, Danbolt NC (2013) GABA and glutamate transporters in brain. *Front Endocrinol (Lausanne)* 4: 165